

Copyright
by
Hyonseok Hwang
2003

The Dissertation Committee for Hyonseok Hwang
certifies that this is the approved version of the following dissertation:

**Electronic Decoherence and Nonadiabatic Chemical
Dynamics in Betaine Dye Molecules**

Committee:

Peter J. Rossky, Supervisor

Paul F. Barbara

John F. Stanton

Jason B. Shear

Gyeong S. Hwang

**Electronic Decoherence and Nonadiabatic Chemical
Dynamics in Betaine Dye Molecules**

by

Hyonseok Hwang, B.S., M.S.

DISSERTATION

Presented to the Faculty of the Graduate School of
The University of Texas at Austin
in Partial Fulfillment
of the Requirements
for the Degree of

DOCTOR OF PHILOSOPHY

THE UNIVERSITY OF TEXAS AT AUSTIN

August 2003

To my late father, my mother, and my sisters

Acknowledgments

One of the things that I value most about my stay in Austin is the nice people that I have had the chance to meet.

First of all, I would like to thank my Ph.D. adviser, Peter J. Rossky, who always showed me the way of thinking and doing on scientific issues and encouraged and stimulated me when I was frustrated or lost.

I also wish to thank the late professor William C. Gardiner. Although I knew him for a short time, I will never forget him.

I owe many thanks to my lab members; Daren Lockwood, Kim F. Wong, Sandro Roberto Possatti da Rocha, Hyojoon Kim, Matt Stone.

Finally, without my mother and my sisters, I would never have reached this stage.

Electronic Decoherence and Nonadiabatic Chemical Dynamics in Betaine Dye Molecules

Publication No. _____

Hyonseok Hwang, Ph.D.
The University of Texas at Austin, 2003

Supervisor: Peter J. Rossky

The effect of electronic decoherence on nonadiabatic (NA) transition rate is investigated with nuclear overlap/phase function (NOPF) and mixed quantum/classical molecular dynamics (MQC-MD) simulations are performed to obtain the NA transition rate on betaine dye molecules. First of all, spin-boson model with ohmic spectral density is used to explore electronic decoherence. We obtain a decoherence function by comparing two solutions for the canonical NOPF based on quantum mechanical and mixed quantum/classical methods, respectively. We provide an electronic decoherence time under short time and high temperature limits. Secondly, electronic decoherence only induced by intramolecular vibrational motions is studied with the NOPF in the simplest betaine molecule, pyridinium-N-phenoxide betaine [4-(1-pyridinio)phenolate]. Decoherence times from several approximations are obtained, including the role of frequency shifts and Duschinsky rotation. We find that the low frequency torsional motion does not make any significant

contribution to the decay of the NOPF. Frequency shifts have more effect on the decay of the NOPF, than Duschinsky rotation does, but the simplest spin-boson model alone describes coherence decay quite well. At longer times, we observe an exponential decay modulated by phase recurrence, but the contribution of the exponential decay to the relaxation is small. Calculated ultrafast decoherence time scales from intramolecular vibrational motions indicate that nuclear motions in solute can have more influence on the total electronic decoherence than does solvent. Thirdly, Frank-Condon (FC) density function in the simplest betaine molecule is calculated, combining the sum-over-states method and the time-dependent method. The FC density function for harmonic vibrational modes is computed by a modified three level-fixed binary tree algorithm including the role of frequency shifts and Duschinsky rotation. For the torsional mode, FC density is computed with the time-dependent method. We find that frequency shifts affect FC density function more than Duschinsky rotation does. The lack of a strong exponential decay in the high frequency region of the FC density function implies that the vibrational motions in the simplest betaine fall onto the strong coupling limit. Finally, Nuclear NA coupling matrix elements by intramolecular vibrational motions are analytically calculated with the spin-boson model. Limitations and applications of the calculation are discussed.

Table of Contents

Acknowledgments	v
Abstract	vi
List of Tables	xi
List of Figures	xii
Chapter 1. About a relationship between electronic decoherence and electronic pure dephasing	1
1.1 Introduction	1
1.2 General derivation of canonical nuclear overlap/phase function	4
1.3 Comparison between a FQM and a MQC result for canonical nuclear overlap/phase function	7
1.4 Derivation of decoherence time from the Wigner distribution function	15
1.5 Summary	17
Chapter 2. Electronic decoherence induced by intramolecular vibrational motions in a betaine dye molecule	19
2.1 Introduction	19
2.2 Theoretical methods	25

2.2.1	Harmonic potential approximation with frequency changes and Duschinsky rotation	28
2.2.2	Torsional motion	31
2.3	Results and Discussion	35
2.3.1	Geometry optimizations and normal mode analysis . . .	35
2.3.2	Nuclear overlap/phase function, $J(t)$	38
2.4	Concluding remarks	51
 Chapter 3. Harmonic model description of the Franck-Condon density for a betaine dye molecule		54
3.1	Introduction	54
3.2	Theoretical methods	59
3.2.1	Franck-Condon density function for harmonic motions with frequency shifts and Duschinsky rotation matrix .	61
3.2.2	Franck-Condon density function induced by torsional mo- tion	68
3.3	Results and discussion	70
3.4	Concluding remarks	80
 Chapter 4. Derivation of quantum mechanical nuclear nonadi- abatic coupling matrix elements using a spin-boson model		85
4.1	Introduction	85
4.2	Quantum mechanical derivation of nuclear nonadiabatic cou- pling matrix elements	87

Bibliography	95
Vita	105

List of Tables

2.1	60 normal mode frequencies (cm^{-1}) and displacements in the ground and the first excited state ^a	53
2.2	Various electronic decoherence times ^a	53
3.1	Comparison between the computational experimental data for low frequency, high frequency, and total intramolecular reorganization energies for simplest betaine and betaine-30 ^a	84
3.2	60 normal mode frequencies (cm^{-1}) and displacements in the ground and the first excited state under the symmetries ^{a,b}	84

List of Figures

2.1	Molecular geometry and atom labelings of pyridinium-N-phenoxide betaine [4-(1-pyridinio)phenolate].	23
2.2	Optimized geometries of the ground (a) and first excited (b) state of the betaine molecule. The upper ring is the pyridinium and the lower the phenoxide ring. In (a), the torsional angle is 41.7° . In (b), the torsional angle is 90° , and the tilt angle of the pyridinium ring is 12.2°	36
2.3	Duschinsky matrix elements between the ground (S_0) and the first excited (S_1) state. To see solely coupling strengths, absolute values of the elements are shown, namely $ D_{ij} $. The numbering is the same as in Table 2.1	39
2.4	Comparison between $ J^{har}(t) $ and $ J^{tor}(t) $. The temperature is held at 8 K to satisfy the low temperature limit.	40
2.5	Comparison among several models for $ J(t) $. Model I includes Duschinsky rotation as well as frequency shifts and displacements. In model II, Duschinsky rotation is not considered. In model III (spin-boson model), only displacements are taken into account. The temperature is the same as in Figure 2.4.	42

2.6	Comparison between $ J(t) $ and $ J^{ga}(t) $. The calculation for $ J^{ga}(t) $ is based on Eq. (2.30). Frequency shifts and Duschinsky rotation are included.	44
2.7	(a) The long time behavior of $ J(t) $. Phase recurrence is seen at around 20 fs. (b) Comparison between $ J(t) $ and $ J^{exp}(t) $. The calculation for $ J^{exp}(t) $ is based on Eq. (2.32). Frequency shifts and Duschinsky rotation are included.	46
2.8	Decays of $ J(t) $ and $\text{Re}\{C(t)\}$. Frequency shifts and Duschinsky rotation are included.	48
3.1	Molecular geometry and atom labelings of pyridinium-N-phenoxide betaine [4-(1-pyridinio)phenolate].	58
3.2	Absolute values of Duschinsky matrices' elements. (a) Normal modes in the ground (S_0) and the first excited state (S_1) are arranged in terms of the increasing order of frequencies. (b) Same as (a) except for being sorted by symmetry first, and then by frequency within the same symmetry. In (b), the modes 1 - 37 belong to symmetry A' and 38 - 60 to symmetry A''	71
3.3	FC densities for the harmonic motions in the resolution of 300 cm^{-1} and 50 cm^{-1} . The inset shows the FC density in the resolution of 1 cm^{-1} . Both frequency shifts and Duschinsky rotation are included	73

3.4	Semilogarithmic plot for the FC density functions comparing between the sum-over-states method and the time-dependent method for the harmonic motions. Both frequency shifts and Duschinsky rotation are included, and $\delta\omega = 300 \text{ cm}^{-1}$	75
3.5	Comparison among several models for $\Sigma^{har}(\omega)$. Model I includes Duschinsky rotation and frequency shifts as well as displacements. In model II, Duschinsky rotation is not considered. Model III only has the effect of displacements. Both frequency shifts and Duschinsky rotation are included, and $\delta\omega = 300 \text{ cm}^{-1}$	77
3.6	The total FC density, $\Sigma^{tot}(\omega)$ along with $\Sigma^{har}(\omega)$ and $\Sigma^{tor}(\omega)$. Both frequency shifts and Duschinsky rotation are included for $\Sigma^{har}(\omega)$, and $\delta\omega = 300 \text{ cm}^{-1}$	79
3.7	Semilogarithmic plot for the FC density function and exponential fit in the high frequency region to observe the exponential decay. For the easy calculation of vibrational reorganization energy, we use the spin-boson model for the FC density function. $\delta\omega = 300 \text{ cm}^{-1}$	81

Chapter 1

About a relationship between electronic decoherence and electronic pure dephasing

1.1 Introduction

In full quantum mechanical (FQM) dynamics, nuclear wave functions evolving on alternative electronic potential energy surfaces (PES) diverge from each other. This so-called electronic decoherence is associated with the decay of off-diagonal elements in a reduced density matrix. [1–3] Electronic decoherence, however, should be distinguished from electronic pure dephasing, which also decay the off-diagonal elements in the reduced density matrix. Electronic pure dephasing is associated with electronic energy gap fluctuations and increases with increasing temperature due to fluctuations while electronic decoherence becomes weak with rising temperature. [4]

There have been several studies on the qualitative relationship between electronic decoherence and pure electronic dephasing, [5] but few studies have been fulfilled on the quantitative relationship between them. [6] It is important to reveal the quantitative relationship between them for a couple of reasons. First of all, this relationship can identify the origin of the decay of the off-diagonal elements in a reduced density matrix more clearly. Since both the electronic decoherence and the pure electronic dephasing can destroy the off-diagonal elements, sometimes it is not clear which one gives more contribution

to the decay. Using the quantitative relations, we can indicate the source of the decay. Secondly, the relationship will provide a theoretical criterion on whether or not a decoherence time should be implemented into an mixed quantum/classical simulation. When the electronic pure dephasing decays much faster than the electronic decoherence, the implementation of the electronic decoherence time into an mixed quantum/classical molecular dynamics (MQC-MD) simulation is not needed. As a result, comparing the two time scales can help determine whether or not a decoherence time should be used in an MQC-MD simulation.

A couple of methods to incorporate decoherence times into MQC-MD simulations dynamically have been proposed and used. [7–10] In those methods decoherence times are provided during the evolution of a system. However, we can think of a different approach to electronic decoherence, where the electronic decoherence is not provided during the evolution, but provided from the initial nuclear distribution. [5] For a thermally equilibrated initial state, MQC methods use the classical Maxwell-Boltzmann distribution to define an initial configuration. Considering that electronic decoherence is a pure quantum effect, we can employ one of quantum statistical representations for the initial distribution to show whether or not using the quantum distribution function yields an electronic decoherence. Among those quantum statistical representations is the canonical Wigner distribution. [11] Lockwood *et al* combined the high temperature result of the canonical Wigner distributions function for the harmonic oscillators with the classical form of the thermally averaged nuclear overlap/phase function (NOPF). They showed that an electronic decoherence

can be realized by using the the Wigner distribution function.

The first purpose of the present study is to present a quantitative relationship between electronic decoherence and electronic dephasing. For this purpose, we employ a two level electronic system linearly coupled with a harmonic bath, so-called spin-boson model. This spin-boson model has been extensively used to explain the system-bath couplings analytically or numerically. We also use the ohmic spectral density to describe the dynamics of the bath. Using the thermally averaged NOPF, we will elucidate a relationship between electronic decoherence and electronic pure dephasing. In addition, we provide a relationship between the electronic decoherence and the solvation relaxation time and show that relationship can be used to estimate an electronic decoherence time. Next we will investigate electronic decoherence induced by the canonical Wigner distribution in MQC methods and explain how the Wigner distribution can provide an electronic decoherence.

The next section shows a general derivation for canonical nuclear overlap/phase function based on the spin-boson model. In section 1.3, an electronic decoherence time and an electronic dephasing time are provided under the high temperature limit and the short-time approximation, and a relationship between those two times are discussed. A solvation relaxation time within the same limit and approximation is calculated as well, and a relationship between the decoherence time and the solvation relaxation time is compared with a previous result by Prezhdo and Rossky. section 1.4 deals with the electronic decoherence provided by combining the Wigner distribution into the MQC method. We make a summary and conclusions on our study in the final

section.

1.2 General derivation of canonical nuclear overlap/phase function

We begin by considering two electronic surfaces which are harmonic in the nuclear coordinates and differ only by displacement of the equilibrium nuclear positions. That is to say, the two electronic states are the subsystem of particular interest and the nuclei are harmonic bath. Much literature on reactions has been devoted to consideration of this spin-boson model [12] or displaced harmonic oscillator model, [13] due to the fact that the analytical expression for physical quantities can be obtained. Suppose that the Hamiltonian of a system is

$$\hat{H} = |i\rangle\hat{H}_i\langle i| + |f\rangle\hat{H}_f\langle f| + \hat{\gamma}^\dagger|i\rangle\langle f| + \hat{\gamma}|f\rangle\langle i|, \quad (1.1)$$

where $|i\rangle$ denotes the initial electronic state and $|f\rangle$ the final electronic state. The electronic coupling matrix element is denoted by $\hat{\gamma}$, while \hat{H}_i and \hat{H}_f are the nuclear Hamiltonians on electronic surfaces $|i\rangle$ and $|f\rangle$, respectively

$$\hat{H}_i = \sum_j \frac{1}{2} \hbar \omega_j \hat{p}_j^2 + \sum_j \frac{1}{2} \hbar \omega_j \hat{q}_j^2, \quad (1.2a)$$

$$\hat{H}_f = \sum_j \frac{1}{2} \hbar \omega_j \hat{p}_j^2 + \sum_j \frac{1}{2} \hbar \omega_j (\hat{q}_j - \Delta_j)^2 + \hbar \omega_0. \quad (1.2b)$$

Here, the index j denotes each nuclear coordinate, with frequency ω_j , coordinate displacement between two states specified by Δ_j , and an energy splitting specified by ω_0 . Dimensionless p_j and q_j are used for convenience.

The dynamics of an electronic subsystem can be expressed in terms of a reduced density matrix $\rho(t)$. [1, 14] For our two-level system, we can write the matrix evolving from an initial condition as

$$\rho(t) = \begin{pmatrix} |c_i(t)|^2 & c_i(t)c_f^*(t)J^*(t) \\ c_i^*(t)c_f(t)J(t) & |c_f(t)|^2 \end{pmatrix}, \quad (1.3)$$

where $c_i(t)$ and $c_f(t)$ are the amplitudes of the electronic wave functions in the initial and final states, respectively, and the nuclear overlap/phase function is given as

$$J(t) = \langle \Psi_i(t) | \Psi_f(t) \rangle, \quad (1.4a)$$

$$= \langle \Psi_i(0) | \exp_+ \left[-\frac{i}{\hbar} \int_0^t d\tau \Delta \hat{H}_{fi}(\tau) \right] | \Psi_i(0) \rangle. \quad (1.4b)$$

Here \exp_+ represents the time-ordered exponential, $\Psi_i(0)$ is an initial nuclear wave function, and $\Delta \hat{H}_{fi}(t)$ is

$$\Delta \hat{H}_{fi}(t) = \exp \left[\frac{i}{\hbar} \hat{H}_i t \right] \Delta \hat{H}_{fi} \exp \left[-\frac{i}{\hbar} \hat{H}_i t \right], \quad (1.5)$$

where $\Delta \hat{H}_{fi} = \hat{H}_f - \hat{H}_i$.

We invoke a decorrelation assumption between the electronic and nuclear parts due to the difference of their time scales. With the thermally equilibrated initial nuclear configuration, the resulting expression for canonical nuclear overlap/phase function $\langle J(t) \rangle_T$ is

$$\langle J(t) \rangle_T = \left\langle \exp_+ \left[-\frac{i}{\hbar} \int_0^t d\tau \Delta \hat{H}_{fi}(\tau) \right] \right\rangle_T, \quad (1.6)$$

where $\langle \dots \rangle_T$ represents thermal averaging over nuclear configurations.

We next perform a cumulant expansion [15] of Eq. (1.6) to obtain

$$\langle J(t) \rangle_T = \exp \left[\sum_{n=1}^{\infty} K_n(t) \right], \quad (1.7)$$

where $K_n(t)$ of Eq. (1.7) is defined as

$$K_n(t) = \left(-\frac{i}{\hbar}\right)^n \int_0^t d\tau_1 \int_0^{\tau_1} d\tau_2 \cdots \int_0^{\tau_{n-1}} d\tau_n \langle \hat{O} \hat{H}_{fi}(\tau_1) \hat{H}_{fi}(\tau_2) \cdots \hat{H}_{fi}(\tau_n) \rangle_c, \quad (1.8)$$

where \hat{O} is the ordering operator, and $\langle \cdots \rangle_c$ represents a cumulant average.

In case that the system is composed of harmonic oscillators, the second order truncation in cumulant expansion gives the exact result. [14] When the truncation is applied to the present model system, the result becomes

$$\langle J(t) \rangle_T = \exp \left[-\frac{it}{\hbar} \langle \Delta \hat{H}_{fi} \rangle_T - \frac{\langle (\delta \hat{U})^2 \rangle_T}{\hbar^2} \int_0^t d\tau_2 \int_0^{\tau_2} d\tau_1 C(\tau_1) \right]. \quad (1.9)$$

In Eq. (1.9), energy gap fluctuation autocorrelation function $C(t)$, which represents the response of the bath to a perturbation, has been introduced [3, 16, 17] and is defined here as

$$C(t) = \frac{\langle \delta \hat{U}(t) \cdot \delta \hat{U}(0) \rangle_T}{\langle \delta \hat{U}(0) \cdot \delta \hat{U}(0) \rangle_T}, \quad (1.10)$$

where the fluctuation operator of electronic energy gap $\delta \hat{U}(t)$ is given as

$$\delta \hat{U}(t) = \Delta \hat{H}_{fi}(t) - \langle \Delta \hat{H}_{fi} \rangle_T. \quad (1.11)$$

Since electronic decoherence is associated with the decay of the norm of $\langle J(t) \rangle_T$, and the solution of Eq. (1.9) in the present model system (spin-boson model) can be obtained elsewhere, [12, 18] we just show the final form of the norm here as

$$|\langle J(t) \rangle_T| = \exp \left[-\int_0^\infty d\omega \rho(\omega) \frac{\coth(\beta \hbar \omega / 2)(1 - \cos(\omega t))}{\omega^2} \right], \quad (1.12)$$

where $\beta = 1/k_B T$ and spectral density $\rho(\omega)$ is introduced as

$$\Omega(\omega) = \sum_j \frac{1}{2} \Delta_j^2 w_j^2 \delta(\omega - \omega_j). \quad (1.13)$$

The spectral density introduced in Eq. (1.13) represents the coupling of bath degrees of freedom to the subsystem. To describe the dynamics occurring in condensed phases properly, several forms for the spectral density have been proposed. [12] In this study, we use the ohmic spectral density, which is given as

$$\Omega(\omega) = \eta \omega \exp \left[-\frac{\omega}{\omega_c} \right], \quad (1.14)$$

where ω_c is a cutoff frequency and η is a classically measurable friction coefficient of the bath.

1.3 Comparison between a FQM and a MQC result for canonical nuclear overlap/phase function

The incorporation of the ohmic spectral density into the Eq. (1.12) leads to [19, 20]

$$|\langle J^{qm}(t) \rangle_T| = \exp \left[-\eta \left\{ \frac{1}{2} \ln(1 + (\omega_c t)^2) + \ln \prod_{n=1}^{\infty} \left[1 + \frac{(\omega_c t)^2}{(1 + n\beta\hbar\omega_c)^2} \right] \right\} \right], \quad (1.15a)$$

$$= \exp \left[-\eta \left\{ \frac{1}{2} \ln(1 + \omega_c^2 t^2) + 2 \ln \Gamma \left(1 + \frac{1}{\beta\hbar\omega_c} \right) - 2 \ln \left| \Gamma \left(1 + \frac{1 + i\omega_c t}{\beta\hbar\omega_c} \right) \right| \right\} \right], \quad (1.15b)$$

where superscript qm is used to distinguish the FQM solution with other solutions from CL or MQC methods which is shown below.

Although Eq. (1.15) is the exact solution, it is difficult to single out terms associated with decoherence. Since the decoherence is only explained by the quantum mechanical description of the nuclear motions, the decoherence can be obtained by comparing the exact quantum solution and the MQC solution of $|\langle J(t) \rangle_T|$. To do so, a mixed quantum-classical limit of Eq. (1.15) is invoked, and the differences between them are explored.

In MQC methods, electronic parts are described quantum mechanically, but nuclear motions are treated classically. $\Delta\hat{H}_{fi}(t)$ is not an operator, but a time-dependent variable. In this case $|\langle J^{mqc}(t) \rangle_T|$ becomes

$$\langle J^{mqc}(t) \rangle_T = \left\langle \exp \left[-\frac{i}{\hbar} \int_0^t d\tau \Delta H_{fi}^{mqc}(\tau) \right] \right\rangle_T, \quad (1.16)$$

where $\Delta H_{fi}^{mqc}(t)$ is

$$\begin{aligned} \Delta H_{fi}^{mqc}(t) = & - \sum_j \hbar\omega_j \Delta_j \{q_j(0) \cos(\omega_j t) + p_j(0) \sin(\omega_j t)\} \\ & + \sum_j \frac{1}{2} \hbar\omega_j \Delta_j^2 + \hbar\omega_0. \end{aligned} \quad (1.17)$$

Inserting Eq. (1.17) into Eq. (1.16) and integrating with respect to time, $\langle J^{mqc}(t) \rangle_T$ along with the classical initial distribution function is finally obtained as

$$|\langle J^{mqc}(t) \rangle_T| = \exp \left[-\eta \left\{ \frac{2t}{\beta\hbar} \tan^{-1}(\omega_c t) - \frac{1}{\beta\hbar\omega_c} \ln(1 + (\omega_c t)^2) \right\} \right], \quad (1.18)$$

where the classical distribution function is given as

$$\rho_{cl}(\mathbf{p}, \mathbf{q}) = \prod_j \frac{\beta \hbar \omega_j}{2\pi} \exp \left[-\frac{\beta \hbar \omega_j}{2} (p_j^2 + q_j^2) \right], \quad (1.19)$$

where $\mathbf{p} = \{p_1, \dots, p_n\}$ and $\mathbf{q} = \{q_1, \dots, q_n\}$.

Taking the high temperature approximation of Eq. (1.15b) leads to Eq. (1.18) since the quantum effects of nuclear motions are suppressed at high temperature, and classical mechanics suffices to describe the nuclear dynamics.

Since there is no nuclear quantum effect in the MQC methods, the decay of $|\langle J^{mqc}(t) \rangle_T|$ is only caused by the electronic pure dephasing. To obtain a dephasing time, we take a short-time limit. Then $|\langle J^{mqc}(t) \rangle_T|$ is approximated as

$$|\langle J^{mqc}(t) \rangle_T| \approx \exp \left[-\frac{t^2}{2\tau_{dp}^2} \right], \quad (1.20)$$

where a dephasing time in the short-time approximation is given as

$$\tau_{dp} = \sqrt{\frac{\beta \hbar}{2\eta\omega_c}}. \quad (1.21)$$

In Eq. (1.21) we can see that the electronic pure dephasing time scale is proportional to the $T^{-1/2}$, i.e. the electronic pure dephasing time decreases with increasing temperature. The electronic pure dephasing time is also related to the energy gap fluctuation. Using the linear response theory, we can express the energy gap fluctuation as

$$\langle \delta \hat{U}^2 \rangle_T = \frac{2\lambda}{\beta}, \quad (1.22)$$

where the reorganization energy λ is obtained from the linear response theory and given in the ohmic bath as

$$\lambda = \eta \hbar \omega_c. \quad (1.23)$$

Eq. (1.21) can be rewritten with Eq. (1.22) as

$$\tau_{dp} = \frac{\hbar}{\sqrt{\langle \delta \hat{U}^2 \rangle_T}}. \quad (1.24)$$

Eq. (1.24) clearly shows that the electronic pure dephasing is associated with the energy gap fluctuation. Eq. (1.21) and Eq. (1.24) together state that the increasing temperature will give rise to the augmentation of the energy gap fluctuation and the increasing fluctuation leads to the increase of the electronic pure dephasing.

In fact, the solution for the short-time limit of the $|\langle J^{mqc}(t) \rangle_T|$ is also obtained by using the pure classical method. In classical methods, the energy gap or reaction rate depends only on the initial nuclear configurations. As a result, ΔH_{fi}^{cl} does not depend on time and $\langle J^{cl}(t) \rangle_T$ becomes

$$\langle J^{cl}(t) \rangle_T = \left\langle \exp \left[-\frac{i}{\hbar} \Delta H_{fi}^{cl} t \right] \right\rangle_T, \quad (1.25)$$

where ΔH_{fi}^{cl} is given as

$$\Delta H_{fi}^{cl} = - \sum_j \hbar \omega_j \Delta_j q_j(0) + \sum_j \frac{1}{2} \hbar \omega_j \Delta_j^2 + \hbar \omega_0. \quad (1.26)$$

After averaged classically over nuclear initial positions $q_j(0)$ and combined with the ohmic bath, $|\langle J^{cl}(t) \rangle_T|$ is given as

$$|\langle J^{cl}(t) \rangle_T| = \exp \left[-\frac{t^2}{2\tau_{dp}^2} \right]. \quad (1.27)$$

Eq. (1.20) and Eq. (1.27) share the same result. In the CL and MQC results, it should be noted that the decay of the thermally averaged NOPF ensues from

the thermal average over the phase in the exponents of Eq. (1.25) and Eq. (1.27). Due to the statistical distribution, each trajectory has different initial nuclear positions and momentums and the path of each trajectory and thereby the phase factor in Eq. (1.25) and Eq. (1.16) differs from each other. When we average over all the trajectory to calculate the thermally averaged NOPF, the difference of the phase factors of the trajectories causes the dephasing. Equivalence at the short time of the CL and the MQC results comes from the fact that both methods take the same classical nuclear distributions as an initial condition. However, the dynamics of evolutions on two different PES's are involved in the MQC methods while only one is involved in the CL methods, and this leads to the differences between these two methods.

Now we make an expansion of the FQM result in terms of β . In the limit of $\beta\hbar\omega_c < 1$, Eq. (1.15b) can be written as [19, 21]

$$|\langle J^{qm}(t) \rangle_T| = \exp \left[-\eta \left\{ \frac{2t}{\beta\hbar} \tan^{-1}(\omega_c t) - \frac{1}{\beta\hbar\omega_c} \ln(1 + (\omega_c t)^2) + \frac{1}{6} \beta\hbar\omega_c^3 t^2 + \vartheta(\beta^3, t^2) \right\} \right]. \quad (1.28)$$

We introduce here a decoherence function $D(t)$, which was used to obtain a configuration-dependent decoherence time by Prezhdo and Rossky. The function is given as

$$J^{qm}(t) = J^{mqc}(t)D(t). \quad (1.29)$$

Under the decorrelation assumption, [22] the thermally averaged $\langle J^{qm}(t) \rangle_T$ is expressed as

$$\langle J^{qm}(t) \rangle_T \approx \langle J^{mqc}(t) \rangle_T \langle D(t) \rangle_T. \quad (1.30)$$

and comparing Eq. (1.18) and Eq. (1.28) leads to the norm of that function as

$$|\langle D(t) \rangle_T| = \exp \left[-\frac{1}{6} \beta \eta \hbar \omega_c^3 t^2 + \vartheta(\beta^3, t^2) \right]. \quad (1.31)$$

When we neglect more than the third order in β , the electronic decoherence function becomes

$$|\langle D(t) \rangle_T| \approx \exp \left[-\frac{t^2}{2\tau_{dc}^2} \right], \quad (1.32)$$

where τ_{dc} is a decoherence time [3] in the approximations and given as

$$\tau_{dc} = \sqrt{\frac{3}{\beta \eta \hbar \omega_c^3}}. \quad (1.33)$$

Eq. (1.33) shows that as the temperature increases, the electronic decoherence time scale becomes longer and the electronic decoherence becomes weak. At low temperature, however, the higher order terms of β in Eq. (1.31) will become dominant, and they should be considered.

From Eq. (1.21) and Eq. (1.33), we can obtain a relationship between the electronic decoherence time and the electronic pure dephasing time under the short-time limit. Comparing τ_{dc} and τ_{dp} leads to

$$\frac{\tau_{dc}}{\tau_{dp}} = \frac{\sqrt{6}}{\hbar \omega_c \beta} = \sqrt{6} \frac{(2\pi/\omega_c)}{h\beta}. \quad (1.34)$$

Here we have two time scales $2\pi/\omega_c$ and $h\beta$ from Eq. (1.34) which are corresponding to the electronic decoherence time and the electronic pure dephasing time, respectively. Reichman and Silbey [18] called the former time scale the "mechanical" time scale and the latter the "quantum-thermal" time scale. $2\pi/\omega_c$ represents the fastest time scale in the system, which shows the largest

quantum effect. The electronic decoherence time, which is a pure quantum effect, will then be governed by this time scale. The second time scale $h\beta$ depends on the temperature. As temperature rises, the second time scale becomes short and significant, which indicates that the second time scale is really associated with the electronic pure dephasing.

In the low temperature where $2\pi/\omega_c < h\beta$, the quantum-thermal time scale becomes longer and accordingly, the electronic pure dephasing becomes slower than the electronic decoherence time. The decay of $\langle J^{qm}(t) \rangle_T$ will then be governed first by the faster electronic decoherence followed by the slower electronic pure dephasing time. In fact, Reichman and Silbey [18] showed that $\langle J^{qm}(t) \rangle_T$ decays exponentially due to the electronic pure dephasing in the low temperature and the long-time limits, namely

$$|\langle J^{qm}(t) \rangle_T| \approx \left(\frac{\beta \hbar \omega_c}{2\pi} \right)^{-\eta} \exp \left[- \frac{\pi \eta t}{\beta \hbar} \right]. \quad (1.35)$$

One may wonder that the exponential decay in Eq. (1.35) is really caused by the electronic pure dephasing. One way to prove that is to investigate the long-time behavior of the $\langle J^{mqc}(t) \rangle_T$ since the decay of $\langle J^{mqc}(t) \rangle_T$ is solely governed by the electronic pure dephasing. If the long-time behavior of $\langle J^{mqc}(t) \rangle_T$ shows the same trend, we can speculate that the electronic pure dephasing leads to the exponential decay in the long time in the low temperature limit. When we calculate the long-time limit of $\langle J^{mqc}(t) \rangle_T$ from Eq. (1.18), we obtain

$$|\langle J^{mqc}(t) \rangle_T| \approx \exp \left[- \frac{\pi \eta t}{\beta \hbar} \right]. \quad (1.36)$$

Even if the pre-exponential factors in Eq. (1.35) and Eq. (1.36) are different,

both have the same exponential decay rate and this proves that the exponential decay is really induced by the electronic pure dephasing.

In the room temperature where the electronic pure dephasing (or quantum-thermal) time scale is around 160 fs, if the decoherence (or mechanical) time is much larger than the electronic pure dephasing time scale, the decay of $\langle J^{qm}(t) \rangle_T$ is mainly caused by the electronic pure dephasing. In real solutions, however, there are in general high frequency nuclear motions in the condensed phase. For example, asymmetric stretching vibrations of water molecules whose time scale is about 9 - 10 fs are involved in the electronic relaxation of a hydrated electron. [23] In this case, the electronic decoherence will occur much faster than the electronic pure dephasing, and the electronic decoherence will account for the most decay of $\langle J^{qm}(t) \rangle_T$. [9, 10]

The real part of $C(t)$ in Eq. (1.10) is related to the experimental fluorescence Stokes shift function, [24] and in the limit where $\beta\hbar\omega_c < 1$ it is approximated in the ohmic bath as [25]

$$\text{Re}\{C(t)\} \approx \frac{1}{1 + \omega_c^2 t^2}. \quad (1.37)$$

Stratt and Cho [17] showed that generally $\text{Re}\{C(t)\}$ can be written as a Gaussian form in the short time limit, here $\omega_c t \ll 1$:

$$\begin{aligned} \text{Re}\{C(t)\} &\approx \frac{1}{1 + \omega_c^2 t^2} = 1 - \omega_c^2 t^2 + \dots, \\ &\approx \exp\left[-\omega_c^2 t^2\right] = \exp\left[-\frac{t^2}{2\tau_g}\right]. \end{aligned} \quad (1.38)$$

where the Gaussian solvation time scale τ_g is given as

$$\tau_g = \frac{1}{\sqrt{2}\omega_c}. \quad (1.39)$$

Comparison between τ_{dc} and τ_g leads to

$$\left(\frac{\tau_{dc}}{\tau_g}\right)^2 = \frac{6}{\beta\eta\hbar\omega_c} = \frac{6}{\beta\lambda}, \quad (1.40)$$

Prezhdo and Rossky have showed the same relation between τ_{dc} and τ_g . [3] In their study, $\langle J^{qm}(t) \rangle_T$ has been calculated using the frozen Gaussian approximation [26–28] and the τ_{dc} has been obtained in the short-time limit. Eq. (1.40) shows that the relationship between τ_{dc} and τ_g depends solely on the quantities that can be gained experimentally. Since the τ_g is also a measurable quantity, the relationship can be used to estimate an electronic decoherence time τ_{dc} . [3]

1.4 Derivation of decoherence time from the Wigner distribution function

In this section, we show how the decoherence time appears from the combination of the canonical Wigner distribution and MQC methods using the spin-boson model with the ohmic spectral density.

The canonical Wigner distribution function is well known for the harmonic oscillator model. [14] When we use the Eq. (4.3a) as the initial Hamiltonian, the Wigner distribution function is given as

$$\rho_W(\mathbf{p}, \mathbf{q}) = \prod_j \frac{\tanh(\beta\hbar\omega_j/2)}{\pi} \exp \left[-\tanh(\beta\hbar\omega_j/2)(p_j^2 + q_j^2) \right], \quad (1.41)$$

Applying the Wigner distribution to the MQC NOPF of Eq. (1.16) and incorporating the ohmic spectral density into the equation leads to

$$|\langle J^{mqc}(t) \rangle_T^W| = \exp \left[-\eta \left\{ \frac{2t}{\beta\hbar} \tan^{-1}(\omega_c t) - \frac{1}{\beta\hbar\omega_c} \ln(1 + (\omega_c t)^2) + \frac{1}{6} \beta\hbar\omega_c^3 t^2 + \vartheta(\beta^3, t^2) \right\} \right], \quad (1.42a)$$

$$= \exp \left[-\eta \left\{ \frac{1}{2} \ln(1 + \omega_c^2 t^2) + 2 \ln \Gamma \left(1 + \frac{1}{\beta\hbar\omega_c} \right) - 2 \ln \left| \Gamma \left(1 + \frac{1 + i\omega_c t}{\beta\hbar\omega_c} \right) \right| \right\} \right], \quad (1.42b)$$

where $\langle \dots \rangle_T^W$ represents averaging over nuclear configurations weighted by the Wigner distribution function.

The exponent of Eq. (1.42a) shows the same decoherence term as in Eq. (1.28). Eq. (1.42a) reveals that an MQC-MD simulation with the Wigner distribution can show some decoherence effects. The appearance of electronic decoherence in an MQC method combined with Wigner distribution has also been addressed by Lockwood *et al.* [5] The Wigner distribution function includes the quantum corrections to the classical distribution function, which means that due to the quantum mechanical uncertainty for the nuclear positions and momenta, there are additional distributions to the classical distribution, and therefore the Wigner distribution function is in general broader than the classical distribution function. We have already shown in the previous section that the MQC methods can describe only the electronic pure dephasing.

Then we can conclude that the decoherence function appearing in Eq. (1.42a) is provided by the electronic pure dephasing that is induced by the additional nuclear distribution due to the quantum mechanical uncertainty.

It should be noted that although the magnitude of the MQC NOPF associated with the Wigner distribution function in Eq. (1.42b) is exactly the same as the FQM result in Eq. (1.15), $\langle J^{mqc}(t) \rangle_T^W$ is not the same as the $\langle J^{qm}(t) \rangle_T$ since the phase factor of the $\langle J^{mqc}(t) \rangle_T^W$ and $\langle J^{qm}(t) \rangle_T$ are different. [29] It is also noted that beyond the harmonic potential energy surfaces, even the magnitude of MQC NOPF with Wigner distribution function will differ from the FQM one. [29]

1.5 Summary

In this study, we showed a relationship between an electronic decoherence time and an electronic pure dephasing time under the high temperature and the short-time limits. The spin-boson model with the ohmic spectral density has been used to calculate the electronic decoherence and the electronic pure dephasing times. The relationship leads to two time scales which are associated with the electronic decoherence and the electronic pure dephasing, respectively. By using those two time scales, we can identify the origin of the off-diagonal elements in a reduced density matrix. The relationship also provide a criterion on the validity of the implementation of a decoherence time into an MQC method.

With the same model, we also showed a relationship between the electronic decoherence time and a solvation time. The relations ship has the same

form as the one proposed by a previous study. [3] Since the relation is expressed with solely with experimental data, we can estimate an electronic decoherence time using the relationship.

We have verified that an MQC method associated with the Wigner distributions can show some electronic decoherence and this electronic decoherence can be considered as an electronic pure dephasing due to the additional nuclear distribution which is caused by the quantum mechanical uncertainty.

Chapter 2

Electronic decoherence induced by intramolecular vibrational motions in a betaine dye molecule

2.1 Introduction

Many chemical processes in condensed phases require using quantum mechanical methods. Among those processes are intra and intermolecular electron transfer (ET) reactions, [30] proton transfer reactions, [31] and electronic relaxation dynamics [32] of a solvated electron. In the case of many degrees of freedom, however, a fully quantum mechanical treatment is intractable since it is required to follow all degrees of freedom in configuration space. One method to address this difficulty is the use of mixed quantum-classical molecular dynamics (MQC-MD) methods where the subsystem (electrons or light particles) degrees of freedom of interest are described with quantum mechanics and the remaining bath (nuclei or heavy particles) degrees of freedom are described classically. [7, 33, 34] However, it has been appreciated that the classical description of bath degrees of freedom can have important and direct impact on observed rate processes. [35] In the full quantum description, loss of subsystem coherence occurs due to the divergence of bath wavefunction evolutions corresponding to alternative quantum states of the subsystem and this divergence is expected to occur very rapidly in condensed phases. [5, 8, 36, 37] For example,

the lack of this so-called decoherence in MQC-MD methods introduces a large hydrogen isotope effect into the relaxation dynamics of the solvated electron, in contrast to experiment. [38]

We will use the term an electronic decoherence to distinguish its quantum nature from electronic pure dephasing; the latter is associated with electronic energy gap fluctuation and appears in all MQC-MD methods. [4] Both electronic decoherence and pure dephasing have an influence on nonadiabatic (NA) transitions by leading to decay of off-diagonal elements of the electronic reduced density matrix, but the electronic decoherence time increases with increasing temperature while the dephasing time decreases with increasing temperature due to the rise of fluctuation. [5, 39]

The understanding of decoherence is of importance in that it not only gives a better insight into phenomena occurring in condensed phases, but also provides a way to overcome the weakness of MQC-MD methods mentioned above. Of particular interest is the quantitative estimation of a decoherence time since the implementation of the dissipative effects of decoherence into MQC-MD methods requires a reasonable estimation of the time. [9, 10]

As mentioned above, decoherence and pure dephasing gives rise to decay of off-diagonal elements in reduced density matrix. An additional point of interest is the long-time behavior of that decay has long been of interest since it is associated with many spectroscopic phenomena such as zero-phonon line shapes in optical spectra. [40, 41] Using a nonperturbative method, Skinner *et al* showed that the decay at long-time limit is exponential. [42–44] Reichman and Silbey used the ohmic spectral density in a two level system to show that

there is some deviations from the expected exponential behavior for experimentally accessible times in very low temperatures. [18]

One avenue to study decay of off-diagonal elements in reduced density matrix and to obtain a decoherence time is by using a nuclear overlap/phase function (NOPF). The NOPF is the overlap between nuclear wavepackets evolving on different electronic potential energy surfaces (PES). This function is responsible for the decay of off-diagonal elements. [1] The NOPF allows us to directly measure coherence time scales, [14, 28, 45] therefore evaluation of this function with a proper approximation can provide decoherence times for NA transition occurring in condensed phase system. [8] For example, Prezhdo and Rossky used a Gaussian form of NOPF introduced by Neria and Nitzan [28, 45] to develop an approximate equation for decoherence time, and applied the equation to obtain decoherence times for the relaxation of an excited solvated electron in water and heavy water. [8] Lockwood *et al* have used molecular dynamics simulation to find a decoherence time for ET between metal ions in ruthenated azurin in water. [37]

Betaine dye molecules are well known for their distinct absorption bands corresponding to solvent polarities. The absorption band is attributed to the large dipole moment change between the ground and the first excited state which is caused by intramolecular forward ET. Due to their intrinsic property, betaine molecules have long attracted significant experimental [46–53] and computational [54–57] attention. Using transient absorption spectroscopy, Barbara and coworkers [47–50] have studied intramolecular back ET rates occurring in the excited state of the betaine-30 molecule. Zong and McHale [51]

focused on the effects of intramolecular vibrational modes as well as solvents on the relaxation following excitation in betaine-30 using resonance Raman spectroscopy. Among computational studies on that dye molecule, Mente and Maroncelli elucidated solvation dynamics in molecular basis by carrying out Monte Carlo simulations of the betaine-30 dye molecule in various solvent. [55] Lobaugh and Rossky used surface hopping method [7] to investigate the dynamics of the betaine-30 molecule after excitation to the first excited state and to elucidate solvent and intramolecular effects on the absorption spectrum of betaine-30. [56, 57]

In the present study, we focus on quantitative description of a popular molecular probe. The simplest betaine, pyridinium-N-phenoxide betaine [4-(1-pyridinio)phenolate], isolated in the gas phase, is investigated to examine electronic decoherence induced by intramolecular vibrational motions between the ground and the first excited state. Figure 2.1 shows this simplest betaine molecule, consisting of a pyridinium ring and a phenoxide ring, linked by an N-C band.

For most intramolecular vibrational motions, we will employ a harmonic PES, which has extensively been used for vibrational or vibronic spectrum calculations and NA transition rate calculations. [58–60] We include frequency shifts and Duschinsky rotation (mode mixing), which can play an role in vibrational motions. [61–65] This inclusion allows us to study the effects of frequency shifts and Duschinsky rotation on electronic decoherence. In general, a torsional motion cannot be described by a harmonic PES due to the softness and periodicity of that coordinate. In most methods related to a torsional motion,

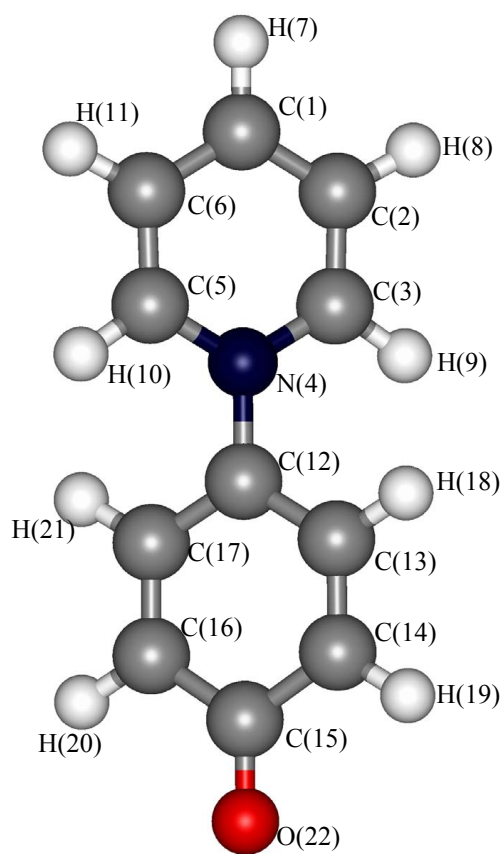


Figure 2.1: Molecular geometry and atom labelings of pyridinium-N-phenoxide betaine [4-(1-pyridinio)phenolate].

a periodic potential energy function for the torsional PES is sought, and the torsional motion is considered as a wave packet evolving on the potential energy function.[66–68] We follow this methodology here, and by doing so, we also study the effect of the torsional motion on decoherence.

We will investigate both the short-time and long-time behavior of the NOPF, which is directly related to the decay of off-diagonal elements in reduced density matrix. [1] We will also use the NOPF to obtain intramolecular motion-induced decoherence times based on alternative approximations. Finally comparing the decoherence times obtained to estimate decoherence times due to solvent nuclear motions, we will be able to examine the contributions of nuclear motions from solute and solvent.

This work is organized as follows. In the following section, we present the theoretical methods to obtain displacements and frequencies for the ground and the first excited state as well as Duschinsky rotation matrix. The detailed procedure to calculate the NOPF is given as well. In section III, the calculated results are shown and discussed. Finally, conclusions are made in section IV.

2.2 Theoretical methods

We begin by considering the ground and the first excited state of a simplest betaine molecule in the gas phase. Of particular interest here is the influence of electronic decoherence on the NA transition from the first excited state to the ground state. Considering the ultrafast time scales of intramolecular vibrational motions, we make the reasonable and conventional [49] assumption that the initial state is the equilibrium geometry in the first excited state. We also use the low temperature limit for calculations, assuming that the excited state vibrations are all in their ground state.

The Hamiltonian of the system composed of these two electronic states can then be expressed in terms of mass-weighted normal coordinates $\mathbf{Q} = \{Q_1, Q_2, \dots, Q_{3N-6}\}$ where N is the number of atoms in the molecule

$$\hat{H} = |g\rangle\hat{H}_g\langle g| + |e\rangle\hat{H}_e\langle e| + \gamma^\dagger|e\rangle\langle g| + \gamma|g\rangle\langle e|, \quad (2.1)$$

where $|g\rangle$ denotes the electronic ground state and $|e\rangle$ the first excited state. γ is an electronic coupling matrix element, while \hat{H}_g and \hat{H}_e are the nuclear Hamiltonians on electronic surfaces $|g\rangle$ and $|e\rangle$, respectively

$$\hat{H}_g = \hat{T}(\dot{\mathbf{Q}}_g) + \hat{V}_g(\mathbf{Q}_g), \quad (2.2a)$$

$$\hat{H}_e = \hat{T}(\dot{\mathbf{Q}}_e) + \hat{V}_e(\mathbf{Q}_e), \quad (2.2b)$$

Here \hat{T} and \hat{V} are the kinetic and the potential energy operators, respectively.

The dynamics of an electronic subsystem can be expressed in terms of a reduced density matrix $\rho(t)$. [1, 14] For our two-level system, we can write

the matrix evolving from the initial conditions stated above as

$$\boldsymbol{\rho}(t) = \begin{pmatrix} |c_e(t)|^2 & c_e(t)c_g^*(t)J^*(t) \\ c_e^*(t)c_g(t)J(t) & |c_g(t)|^2 \end{pmatrix}, \quad (2.3)$$

where $c_e(t)$ and $c_g(t)$ are the amplitudes of electronic wave functions in the first excited and ground states, respectively. The NOPF, $J(t)$ in Eq. (2.3) is given as [8, 14, 45]

$$J(t) = \left\langle \Psi_e(0) \left| \exp \left[\frac{i}{\hbar} \hat{H}_e t \right] \exp \left[- \frac{i}{\hbar} \hat{H}_g t \right] \right| \Psi_e(0) \right\rangle, \quad (2.4)$$

where $\Psi_e(0)$ is the initial nuclear wave function prepared in the equilibrium geometry of the first excited state.

Up to this point, a general description for the NOPF has been provided. We now invoke some reasonable approximations for the calculation of the NOPF for intramolecular vibrational motions. First, harmonic PES are utilized for the other vibrational motions than the torsional motion. In many cases, spin-boson model, [12] which only considers displacements in harmonic potentials is sufficient to describe a system. [69] In general, however, frequency shifts and mixing of modes (Duschinsky rotation) must be taken into account to precisely explain the change of the vibrational normal modes accompanied by an electronic transition. [64, 65] Frequency shifts occur due to force constant differences between two PES's and Duschinsky rotation arises when two electronic states have different vibrational normal mode coordinate systems. We describe how we obtain frequency shifts and Duschinsky rotation matrix in the following subsection. Due to the periodic torsional PES and the large difference between the optimized torsional angles of the two states (see below),

the torsional PES is beyond harmonic potential description. For the torsional motion, we use a method, which has been proposed by Seidner *et al* [66] and used popularly by others. [67, 68] This method will also be described in detail in the second subsection.

We now decompose the nuclear Hamiltonian in Eq. (2.1) into two parts [70]

$$\hat{H} = \hat{H}^{har} + \hat{H}^{tor}, \quad (2.5)$$

where \hat{H}^{har} means the Hamiltonian which describes all the vibrational motions under the harmonic potential approximation and \hat{H}^{tor} represents the Hamiltonian for the torsional motion. The torsional motion decouples from the other modes and can be treated separately if we assume

$$\left[\hat{H}^{har}, \hat{H}^{tor} \right] = 0. \quad (2.6)$$

This approximation is based on the time scale difference between slow torsional motions and other motions. Under this approximation, the NOPF from Eq. (2.4) can be factored into a product, which is given by

$$J(t) = J^{har}(t)J^{tor}(t), \quad (2.7)$$

where $J^{har}(t)$ is the NOPF corresponding to \hat{H}^{har} and $J^{tor}(t)$ corresponding to \hat{H}^{tor} . The detailed expressions for $J^{har}(t)$ and $J^{tor}(t)$ as well as \hat{H}^{har} and \hat{H}^{tor} are provided next.

2.2.1 Harmonic potential approximation with frequency changes and Duschinsky rotation

Here we consider $3N - 7$ vibrational degrees of freedom; the seventh degree of freedom excluded is the torsional degree of freedom. As mentioned above, the initial state is the first excited state and the final state is the ground state, and those two states are coupled through vibrational motions which are expressed by mass-weighted normal coordinates $\mathbf{Q} = \{Q_1, Q_2, \dots, Q_{3N-7}\}$. The nuclear Hamiltonians in the two states, which are assumed to be harmonic, differ by frequency shifts and Duschinsky rotation as well as the displacement of the equilibrium nuclear positions. The Hamiltonian is then given by

$$\hat{H}^{har} = |g\rangle \hat{H}_g^{har}(\mathbf{Q}_g) \langle g| + |e\rangle \hat{H}_e^{har}(\mathbf{Q}_e) \langle e| + \gamma^{har}(|g\rangle \langle e| + |e\rangle \langle g|), \quad (2.8)$$

where γ^{har} is assumed to be real and static and

$$\hat{H}_g^{har}(\mathbf{Q}_g) = \frac{1}{2} \dot{\mathbf{Q}}_g^T \dot{\mathbf{Q}}_g + \frac{1}{2} \mathbf{Q}_g^T \boldsymbol{\Omega}_g \mathbf{Q}_g, \quad (2.9a)$$

$$\hat{H}_e^{har}(\mathbf{Q}_e) = \frac{1}{2} \dot{\mathbf{Q}}_e^T \dot{\mathbf{Q}}_e + \frac{1}{2} \mathbf{Q}_e^T \boldsymbol{\Omega}_e \mathbf{Q}_e + \Delta G. \quad (2.9b)$$

Here $\boldsymbol{\Omega}_e$ and $\boldsymbol{\Omega}_g$ are diagonalized frequency matrices in each state and ΔG is the potential energy minimum difference between two states. \mathbf{Q}^T is the transpose of \mathbf{Q} .

To evaluate the integral of $J^{har}(t)$, we should express the coordinates of the ground state as functions of the coordinates of the first excited state. This can be accomplished by a linear combination [61, 69, 71]

$$\mathbf{Q}_g = \mathbf{D}\mathbf{Q}_e + \Delta\mathbf{Q}, \quad (2.10)$$

where \mathbf{D} means Duschinsky rotation matrix and $\Delta\mathbf{Q}$ represents a displacement vector between the minima of the two states.

There are at least two methods to obtain \mathbf{D} and $\Delta\mathbf{Q}$. [69, 72] In one straightforward approach, geometry optimizations for each electronic state are performed independently. [72–74] but in an alternative method due to Lee *et al.*, [69] the geometry optimization is only carried out for the initial electronic state, and the geometry of the final electronic state is estimated by projecting the force constant matrix (Hessian matrix) at the optimized geometry of the initial state. Due to the difference of the two methods, one obtains different frequencies, \mathbf{D} , and $\Delta\mathbf{Q}$ from each method. When we calculate reorganization energies by intramolecular vibrational motions using each method and compare those reorganization energies to experimental data [49], the reorganization energy obtained from the the straightforward method is unreasonably large while the energy from the other method is acceptable. This results from the relatively large displacements in the present case. We therefore adopt Lee *et al.*'s method [69] for our calculation.

Following Lee *et al.*'s method, [69] we first optimize the excited state and perform frequency analysis of that electronic state to obtain the Ω_e and $3N \times (3N - 7)$ transformation matrix \mathbf{L}_e^{mx} , which transforms mass-weighted Cartesian coordinates into normal coordinates. Next we calculate the Hessian matrix and the mass-weighted force vector (gradient) of the ground state at the equilibrium position of the first excited state. Duschinsky matrix can be evaluated with

$$\Omega_g^2 = \mathbf{D}(\mathbf{L}_e^{mx})^T \mathbf{K}_g^{mx} \mathbf{L}_e^{mx} \mathbf{D}^T. \quad (2.11)$$

Here \mathbf{K}_g^{mx} is the Hessian matrix of the ground state in Cartesian coordinates. In Eq. (2.11), Ω_g^2 and \mathbf{D} can be obtained simultaneously by diagonalizing $(\mathbf{L}_e^{mx})^T \mathbf{K}_g^{mx} \mathbf{L}_e^{mx}$ with the Symmetry Matrix Eigenvalue (SME) method or the Singular Value Decomposition (SVD) method. [75] The mass-weighted displacement vector $\Delta \mathbf{Q}$ is then calculated from

$$\Delta \mathbf{Q} = (\Omega_g^2)^{-1} \mathbf{D} (\mathbf{L}_e^{mx})^T \mathbf{F}_g^{mx}, \quad (2.12)$$

where \mathbf{F}_g^{mx} is the mass-weighted gradient of the ground state PES which is obtained at the equilibrium position of the first excited state. \mathbf{F}_g^{mx} is expressed in terms of Cartesian coordinates.

To obtain $J^{har}(t)$, we will use the finite temperature analytical result, and evaluate the function at very low temperature. The thermally averaged NOPF for harmonic motions $\langle J^{har}(t) \rangle_T$ has an exact solution with the assistance of Kubo-Toyozawa formalism, [59, 69, 76]

$$\langle J^{har}(t) \rangle_T = \exp \left[-\frac{it}{\hbar} \Delta G - f_1(t) - f_2(t) \right], \quad (2.13)$$

where

$$f_1(t) = \Delta \mathbf{Q}^T \Theta_e (\Theta_e + \tilde{\Theta}_g)^{-1} \tilde{\Theta}_g \Delta \mathbf{Q}, \quad (2.14)$$

and

$$f_2(t) = \frac{1}{2} Tr \left[\ln \left\{ \hbar^2 \left(2 \sinh \left(\frac{\beta \hbar \Omega_e}{2} \right) \right)^{-2} \right. \right. \\ \left. \left. \times \Omega_e^{-1} \sinh((\beta \hbar - it) \Omega_e) (\Theta_e + \tilde{\Theta}_g) (\Phi_e + \tilde{\Phi}_g) \Omega_g^{-1} \sinh(i \Omega_g t) \right\} \right]. \quad (2.15)$$

Tr means trace and the matrices above are defined as

$$\Theta_e = \frac{1}{\hbar} \Omega_e \tanh \left\{ \frac{(\beta \hbar - it) \Omega_e}{2} \right\}, \quad (2.16a)$$

$$\Theta_g = \frac{1}{\hbar} \Omega_g \tanh \left\{ \frac{i \Omega_g t}{2} \right\}, \quad (2.16b)$$

$$\Phi_e = \frac{1}{\hbar} \Omega_e \coth \left\{ \frac{(\beta \hbar - it) \Omega_e}{2} \right\}, \quad (2.17a)$$

$$\Phi_g = \frac{1}{\hbar} \Omega_g \coth \left\{ \frac{i \Omega_g t}{2} \right\}, \quad (2.17b)$$

$$\tilde{\Theta}_g = \mathbf{D}^T \Theta_g \mathbf{D}, \quad (2.18a)$$

$$\tilde{\Phi}_g = \mathbf{D}^T \Phi_g \mathbf{D}, \quad (2.18b)$$

and $\beta = 1/k_B T$.

In the case of the spin-boson model, \mathbf{D} becomes the identity matrix and $\Omega_g = \Omega_e = \{\omega_1, \omega_2, \dots, \omega_{3N-7}\}$. As a result, $f_2(t) = 0$ and $\langle J^{har}(t) \rangle_T$ is given as

$$\begin{aligned} \langle J_{SB}^{har}(t) \rangle_T &= \exp \left[- \sum_j^{3N-7} S_j [(\coth(\beta \hbar \omega_j / 2)(1 - \cos(\omega_j t)) + i \sin(\omega_j t))] \right], \\ &\times \exp \left[- \frac{it}{\hbar} \Delta G \right], \end{aligned} \quad (2.19)$$

where S_j is a Huang-Rhys factor and defined as $S_j = \frac{1}{2} \Delta Q_j^2$.

2.2.2 Torsional motion

As mentioned above, the central inter-ring torsional motion is well beyond a harmonic potential description due to a large torsional angle difference

between the optimized geometries of the ground and the first excited state and the periodic torsional PES. In order to examine the torsional motion properly, we explicitly calculate the periodic torsional potential energy function for the torsional motion of the electronic ground state. The torsional dynamics is then described as a wave packet evolving on the periodic PES. The dynamics of that mode is obtained by solving directly the time-dependent Schrödinger equation (TDSE). [66–68]

One usually approximates the Hamiltonian for a torsional motion as [66–68]

$$\hat{H}^{tor} = |g\rangle\hat{H}_g^{tor}(\theta)\langle g| + |e\rangle\hat{H}_e^{tor}(\theta)\langle e| + \gamma^{tor}(|g\rangle\langle e| + |e\rangle\langle g|), \quad (2.20)$$

where γ^{tor} is assumed to be real and static and

$$\hat{H}_g^{tor}(\theta) = -\frac{\hbar^2}{2I^{tor}}\frac{\partial^2}{\partial\theta^2} + V_g^{tor}(\theta), \quad (2.21a)$$

$$\hat{H}_e^{tor}(\theta) = -\frac{\hbar^2}{2I^{tor}}\frac{\partial^2}{\partial\theta^2} + V_e^{tor}(\theta), \quad (2.21b)$$

where θ is the torsional angle between the pyridinium ring and the phenoxide ring and I^{tor} is a reduced moment of inertia. $V_e^{tor}(\theta)$ and $V_g^{tor}(\theta)$ are the torsional PES's of each state.

The reduced moment of inertia I^{tor} for the torsional angle defined about the bond between N(4) atom and C(12) atom in Figure 2.1 is given as [68]

$$I^{tor} = \frac{I_{py}I_{ph}}{I_{py} + I_{ph}}, \quad (2.22)$$

In Eq. (2.22), I_{py} is defined as

$$I_{py} = \sum_j m_j \mathbf{r}_j^2, \quad (2.23)$$

where j means any atom in pyridinium ring and \mathbf{r}_j represents the distance between atom j and the torsional axis. In the same manner, I_{ph} is

$$I_{ph} = \sum_k m_k \mathbf{r}_k^2 \quad (2.24)$$

The initial nuclear wave function is in the equilibrium position of the first excited state. Under this assumption, the harmonic potential can be used for the first excited state PES and the $V_e^{tor}(\theta)$ is given as

$$V_e^{tor}(\theta) = \frac{1}{2} I^{tor} (\omega_e^{tor})^2 (\theta - \theta_0^e)^2, \quad (2.25)$$

where θ_0^e is the torsional angle at the equilibrium configuration of the first excited state and V_0^{tor} is the energy at the configuration.

The harmonic potential, however, cannot be applied to the ground state because the nuclear positions are far from the equilibrium positions of the ground state. In this case, the explicit torsional PES for the ground state is necessary. In general, the PES for the torsional motion is given as [77]

$$V_g^{tor}(\theta) = \frac{1}{2} \sum_n V_n (1 - \cos\{n(\theta - \theta_0^g)\}), \quad (2.26)$$

where θ_0^g is the torsional angle at the equilibrium configuration of the ground state and n is an integer. To obtain parameters for the ground state torsional PES, potential energies are calculated by varying the torsional angle θ and then fitting the energies as a function of θ .

Now $J^{tor}(t)$ can be written as

$$J^{tor}(t) = \langle \Psi_e^{tor}(t) | \Psi_g^{tor}(t) \rangle, \quad (2.27)$$

where $\Psi_e^{tor}(t)$ and $\Psi_g^{tor}(t)$ are obtained by solving the TDSE

$$i\hbar \frac{\partial}{\partial t} \Psi_e^{tor}(t) = \hat{H}_e^{tor} \Psi_e^{tor}(t), \quad (2.28)$$

and

$$i\hbar \frac{\partial}{\partial t} \Psi_g^{tor}(t) = \hat{H}_g^{tor} \Psi_g^{tor}(t). \quad (2.29)$$

When we follow Seidner *et al*'s work, [66] standard fast Fourier transformation (FFT) techniques [78, 79] are used to propagate the wave functions, and the overlap in Eq. (2.27) is integrated with respect to the torsional angle θ . [66–68]

2.3 Results and Discussion

2.3.1 Geometry optimizations and normal mode analysis

Geometry optimizations and frequency analysis are performed with the GAUSSIAN 98 program. [80] The geometry optimization in the ground state is carried out at the Hartree-Fock level at with 6-31G* basis set. Configuration interaction singles (CIS) with the same basis set is used to optimize the first excited state. Frequencies in this paper are scaled with the factor of 0.91. [81] The geometry optimizations of the ground and the first excited state are performed without applying any symmetries at first, and then by applying C_2 symmetry for the ground and C_s for the first excited state. The torsional angle between the pyridinium ring and the phenoxide ring in the first excited state is held fixed at 90° under the C_s symmetry. Since we found that the electronic energies under the symmetries are not significantly different from those without symmetries, we have applied the symmetries in all of our calculations.

Figure 2.2 shows the optimized geometries of the ground state and the first excited state. The central bond lengths between N(4) and C(12) (see Figure 2.1) are 1.42 Å and 1.39 Å in the ground and the first excited state. The optimized torsional angle of 41.7° in the ground is increased into 90° in the first excited state. This angle difference is attributed to the π to π^* transition, and this difference has already been observed by an *ab initio* calculation study. [82, 83] In addition, a tilted geometry of the pyridinium ring is observed in the first excited state. The tilted geometry with the same angle of 12.2° has also been reported by the calculation of Hogiu *et al.* [52]

In Table 2.1, frequencies and dimensionless displacements of 60 vibra-

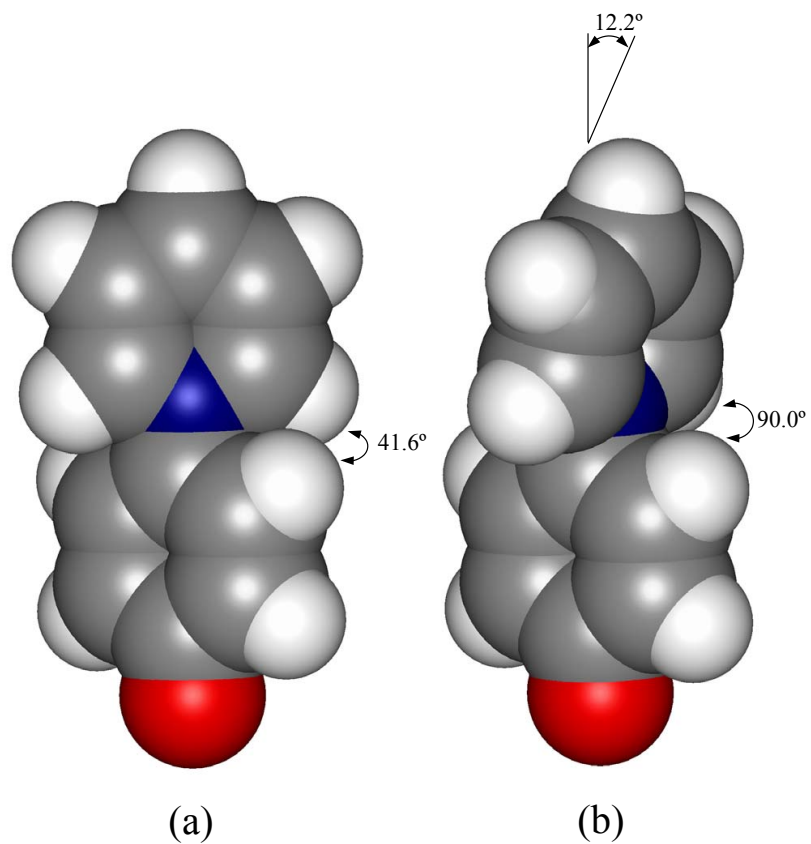


Figure 2.2: Optimized geometries of the ground (a) and first excited (b) state of the betaine molecule. The upper ring is the pyridinium and the lower the phenoxide ring. In (a), the torsional angle is 41.7° . In (b), the torsional angle is 90° , and the tilt angle of the pyridinium ring is 12.2° .

tional modes of the ground and the first excited state are listed, respectively. Among those vibrational modes are 37 totally symmetric vibrational modes and the others are nontotally symmetric modes. Note that only totally symmetric vibrational modes have displacements. [64] The ground state frequencies are calculated by projecting into the normal coordinates of the first excited state the force constant matrix of the ground state and by diagonalizing the matrix. This calculation is performed by using Eq. (2.11). Note that the force constant matrix is obtained at the equilibrium position of the first excited state.

From our vibrational analysis, 56.5 cm^{-1} can be assigned to the frequency of the torsional mode in the ground state and 121.6 cm^{-1} in the first excited state. In the case of the inter-ring stretching mode, 294.4 cm^{-1} is assigned to the ground state and 280.0 cm^{-1} to the first excited state. Note that in Table 2.1, the displacement for the torsional mode is zero despite the large angle difference between the two optimized geometries. This is because the torsional mode in the first excited state is a nontotally symmetric mode, and due to the projection of the force constant matrix into the normal coordinates of the first excited state, the mode in the ground state also becomes a nontotally symmetric mode.

Hogiu *et al* [52] also assigned some frequencies obtained from the Raman spectrum of betaine-30 to the torsional and the stretching mode. In their analysis, they assigned 133 cm^{-1} to the torsional mode and 1209 cm^{-1} to the stretching mode. The peak of 291 cm^{-1} was attributed to the inversion of the pyridinium nitrogen atom in their study. Since each ring in the betaine-30 has

Table 2.1: 60 normal mode frequencies (cm^{-1}) and displacements in the ground and the first excited state^a

mode	ω_g	ω_e	ΔQ	mode	ω_g	ω_e	ΔQ	mode	ω_g	ω_e	ΔQ
1	69.5	28.1	-5.69	21	686.4	745.1	0.00	41	1480.6	1291.5	0.00
2	27.1	62.4	0.00	22	765.9	771.3	0.51	42	1327.2	1344.0	-0.59
3	56.5	121.6	0.00	23	768.4	810.9	0.00	43	1337.5	1370.0	0.00
4	154.0	170.5	0.00	24	838.9	876.7	0.00	44	1452.5	1427.2	0.03
5	282.6	201.5	1.56	25	936.3	953.1	0.28	45	1436.2	1447.7	-0.30
6	294.4	280.0	0.21	26	1025.9	969.0	0.00	46	1477.6	1478.4	0.29
7	369.2	352.0	0.00	27	949.4	969.2	-0.54	47	1522.8	1522.7	0.00
8	512.1	387.5	-0.36	28	1047.3	972.7	0.19	48	1528.0	1535.8	0.06
9	402.6	425.5	0.00	29	1006.6	999.4	0.36	49	1622.7	1620.2	0.02
10	410.0	434.9	0.00	30	1018.6	1008.2	-1.01	50	1670.2	1666.6	-0.99
11	435.7	457.0	-0.75	31	966.6	1018.7	0.00	51	1748.3	1746.3	0.30
12	556.5	538.3	0.19	32	960.8	1020.8	0.00	52	3092.9	3087.0	0.05
13	466.1	544.0	0.00	33	1155.1	1031.4	0.00	53	3094.6	3089.1	0.00
14	616.0	594.8	0.06	34	1115.2	1081.7	0.00	54	3076.7	3102.3	0.06
15	683.7	631.1	-0.39	35	1061.5	1097.1	0.00	55	3074.8	3102.8	0.00
16	620.1	635.3	0.00	36	1145.5	1163.1	-0.16	56	3104.3	3119.7	-0.04
17	804.7	658.3	0.08	37	1201.2	1206.5	0.70	57	3107.0	3121.4	0.06
18	699.4	692.2	0.39	38	1266.3	1252.0	-0.03	58	3145.5	3128.4	0.02
19	1000.7	720.8	-0.05	39	901.7	1261.8	0.00	59	3179.7	3154.4	0.00
20	874.1	737.2	0.00	40	1172.1	1285.0	0.03	60	3181.5	3158.7	0.06

^a Configuration interaction singles (CIS) with 6-31G* is used to perform a geometry optimization for the first excited state. The frequencies of the ground state is obtained at the optimized geometry of the first excited state by diagonalizing force constant matrix (Hessian matrix) of the ground state. Calculation for the force constant matrix is performed at Hartree-Fock level with 6-31G*. Frequency scaling factor is 0.91, and displacements are unitless. See text.

larger mass due to phenyl groups attached to each ring than in the simplest betaine, we believe that 1209 cm^{-1} is too high to be assigned to the inter-ring stretching mode. This issue is discussed further elsewhere. [84]

Figure 2.3 shows the contour map of the absolute values of the Duschinsky matrix elements $|D_{ij}|$ obtained from Eq. (2.11). MOdesa are numbered in order of increasing frequency. Although there are some off-diagonal elements in the low and middle frequency region, the map shows that the matrix is nearly diagonal, which suggests that Duschinsky matrix effect may not be large in this betaine molecule, and that a spin-boson model may be a good approximation. It is also evident that couplings occur largely between normal modes with similar frequencies, and there are more couplings at low frequency modes than at middle or high frequency modes. It is also seen that nine C-H stretching modes of over 3000 cm^{-1} are not coupled to other modes at low or middle frequencies.

2.3.2 Nuclear overlap/phase function, $J(t)$

Figure 2.4 compares the decays of $|J^{har}(t)|$ and $|J^{tor}(t)|$ using the Eqs. (2.13) and (2.27), respectively. In all the calculations of the desired NOPF, we employ the low temperature limit by fixing the temperature at 8 K. At a temperature of 8 K, each normal mode including the torsional mode stays at its vibrational ground state in the first excited state. Figure 2.4 shows that the decay of $|J^{tor}(t)|$ is much slower than that of $|J^{har}(t)|$. The effect of the torsional motion on the electronic decoherence is therefore insignificant when compared with the other vibrational modes.

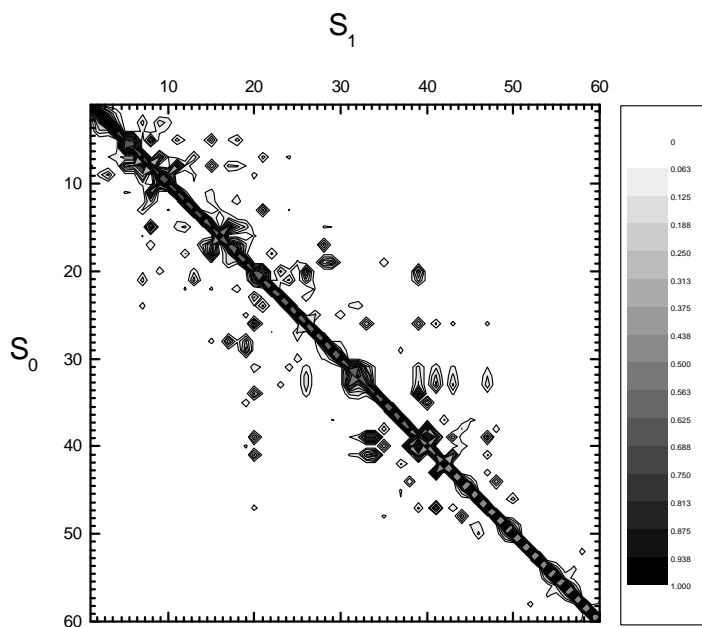


Figure 2.3: Duschinsky matrix elements between the ground (S_0) and the first excited (S_1) state. To see solely coupling strengths, absolute values of the elements are shown, namely $|D_{ij}|$. The numbering is the same as in Table 2.1

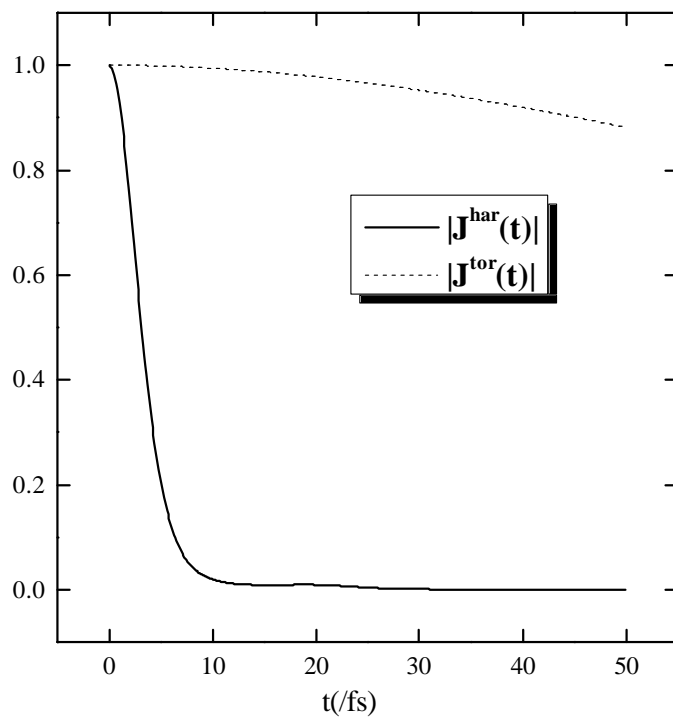


Figure 2.4: Comparison between $|J^{har}(t)|$ and $|J^{tor}(t)|$. The temperature is held at 8 K to satisfy the low temperature limit.

In Figure 2.5, model I includes the effect of Duschinsky rotation as well as frequency shifts and displacements. While frequency shifts and displacements are considered in model II, model III accounts solely for the effect of displacements (spin-boson model). As is evident from Figure 2.5, that model II is somewhat different from model III, the differences originating from frequency shifts in the model II. A comparison between model I and model II shows that Duschinsky rotation has a very minor effect. Based on these observations, in our molecular system, frequency shifts introduce large deviations from the spin-boson model than the Duschinsky rotation does.

However, the differences among those three models are not large. Lee *et al* [69] studied an ET reaction between tryptophan cation radical and tyrosine, comparing reaction rates from those three models, respectively. Their results also demonstrated that both frequency shifts and Duschinsky rotation produced only a minor effect. These limited studies thus suggest that reasonable results should be obtained when using a spin-boson model for polyatomic systems without further modifications such as frequency shifts or Duschinsky rotation.

Prezhdo and Rossky [3, 8] used the frozen gaussian approximation (FGA) to derive decoherence time in the short time limit. In their derivation, the thermally averaged NOPF $|\langle J(t) \rangle_T|$ has the form

$$|\langle J^{ga}(t) \rangle_T| \approx \exp \left[-\frac{1}{2} \frac{t^2}{(\tau_D^{ga})^2} \right], \quad (2.30)$$

The general form of Eq. (2.30) can be written as

$$\tau_D^{ga} = \left[- \left\{ \frac{d^2}{dt^2} \ln |\langle J(t) \rangle_T| \right\}_{t=0} \right]^{-\frac{1}{2}}. \quad (2.31)$$

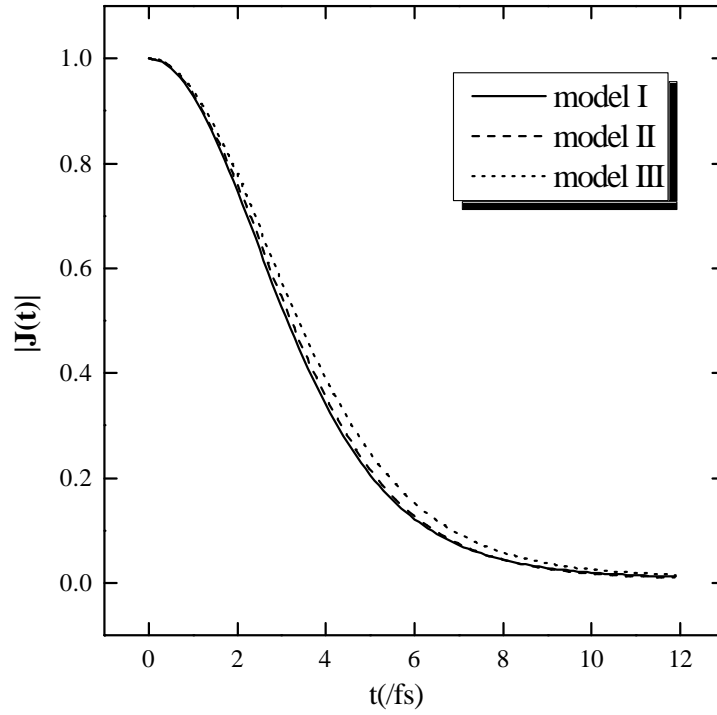


Figure 2.5: Comparison among several models for $|J(t)|$. Model I includes Duschinsky rotation as well as frequency shifts and displacements. In model II, Duschinsky rotation is not considered. In model III (spin-boson model), only displacements are taken into account. The temperature is the same as in Figure 2.4.

Figure 2.6 shows the comparison between the $|J(t)|$ based on Eq. (2.4) and the Gaussian form of $|J(t)|$ based on Eq. (2.30). Since the approximation is made in the short time regime, the approximation is excellent up to 2 fs, when it starts digressing from the correct values. It can be seen, however, that the deviation at long times is not large. Eq. (2.30) is also used to obtain a decoherence time τ_D^{ga} , and the estimated value of τ_D^{ga} by the intramolecular vibrational modes is 2.64 fs. It is interesting to note that Lockwood *et al* found that a decoherence time occurring in a solvated ET protein is 2.4 fs, with the protein alone accounting for a value of 4 fs, a quite comparable value. [5]

Now we investigate the longer time behavior of the canonical NOPF. One phenomenon resulting from the finite number of normal modes in the calculation of the canonical NOPF is phase recurrence, which means that the canonical NOPF does not decay completely. [18, 85, 86] Figure 2.7(a) clearly shows evident phase recurrence. The first recurrence is associated with normal modes which have higher frequency and larger displacements. Table 2.1 shows that the 50th normal mode of which frequency is around 1670 cm^{-1} has a large displacement. The time scale of the first phase recurrence occurring at around 20 fs corresponds to that of this normal mode.

We noted earlier, that theoretical considerations [18, 42–44] imply exponential decay at long times. Even in this 60 mode system, we see in Figure 2.7(a) that decay beyond 5 - 10 fs is roughly exponential. From Figure 2.7(b), we can see that an exponential decay begins at around 4.7 fs. When we use

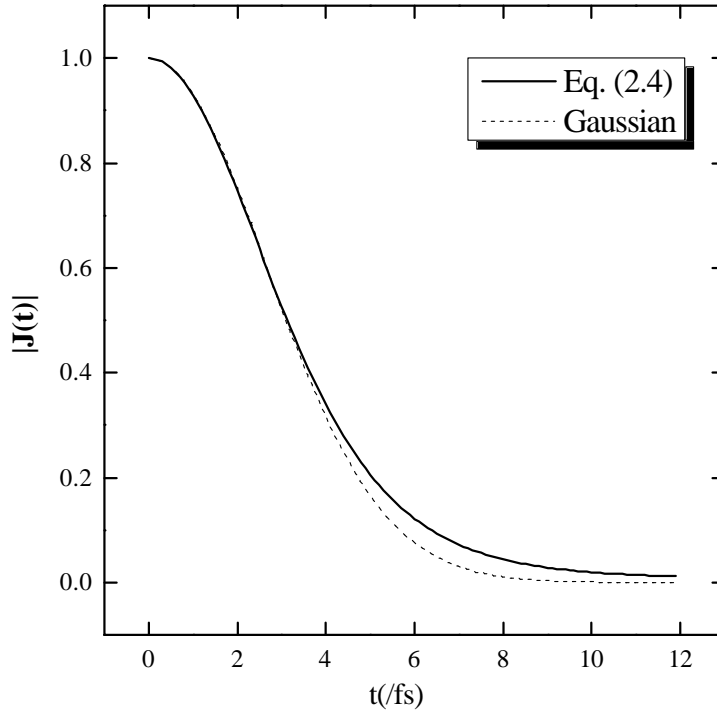


Figure 2.6: Comparison between $|J(t)|$ and $|J^{ga}(t)|$. The calculation for $|J^{ga}(t)|$ is based on Eq. (2.30). Frequency shifts and Duschinsky rotation are included.

an exponential fitting function, for this time regime

$$|J^{exp}(t)| \approx \exp\left[-\frac{t}{\tau_d^{exp}}\right], \quad (2.32)$$

the τ_d^{exp} is estimated as approximately 1.91 fs. However, comparing the exponential decay with the Gaussian (Figure 2.6), we observe that the initial Gaussian decay is dominant. The roughly exponential decay characterizes only the last about 25 %, and the characteristic time scale is comparable.

Now we consider why the exponential decay is weak and less dominant than the initial Gaussian decay in this system. Since the contributions of the torsional motion, frequency shifts, and Duschinsky rotation to the decay of the canonical NOPF is not large, a second order truncation in the cumulant expansion of $|\langle J(t) \rangle_T|$ is a reasonable approximation for the harmonic vibrational motions. Then the result is given as [14, 15]

$$|\langle J(t) \rangle_T| \approx \exp\left[-\frac{\langle(\delta\hat{U})^2\rangle_T}{\hbar^2} \int_0^t dt_2 \int_0^{t_2} dt_1 \text{Re}\{C(t_1)\}\right]. \quad (2.33)$$

Here normalized energy gap fluctuation autocorrelation function $C(t)$ is defined as

$$C(t) = \frac{\langle\delta\hat{U}(t) \cdot \delta\hat{U}(0)\rangle_T}{\langle\delta\hat{U}(0) \cdot \delta\hat{U}(0)\rangle_T}, \quad (2.34)$$

where $\delta\hat{U}(t)$ is defined as

$$\delta\hat{U}(t) = \Delta\hat{H}_{ge}(t) - \langle\Delta\hat{H}_{ge}\rangle_T, \quad (2.35)$$

and $\Delta\hat{H}_{ge}$ is as

$$\Delta\hat{H}_{ge} = \hat{H}_g - \hat{H}_e. \quad (2.36)$$

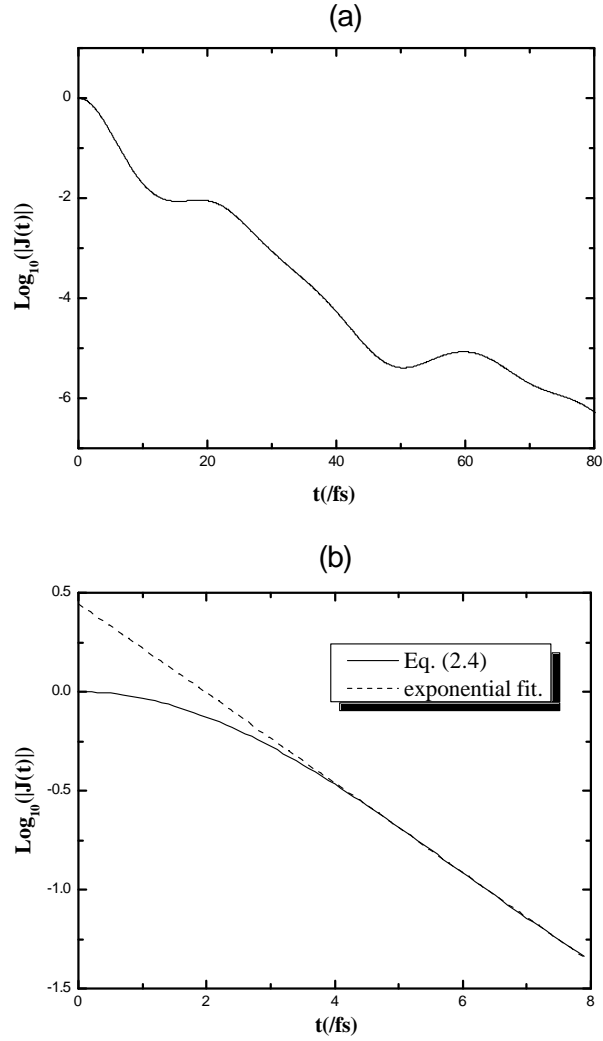


Figure 2.7: (a) The long time behavior of $|J(t)|$. Phase recurrence is seen at around 20 fs. (b) Comparison between $|J(t)|$ and $|J^{exp}(t)|$. The calculation for $|J^{exp}(t)|$ is based on Eq. (2.32). Frequency shifts and Duschinsky rotation are included.

When the normalized $C(t)$ decays completely before a typical correlation time of τ_c , for times $t \gg \tau_c$, Eq. (2.33) can be written as [14, 87, 88]

$$|\langle J(t) \rangle_T| \approx \exp \left[- \frac{\langle (\delta \hat{U})^2 \rangle_T}{\hbar^2} M t \right]. \quad (2.37)$$

where M is defined as

$$M = \int_0^\infty dt_1 \operatorname{Re}\{C(t_1)\}. \quad (2.38)$$

From Eq. (2.37), we see the exponential decay of $|\langle J(t) \rangle_T|$. As a consequence, the first condition for the exponential decay of $|\langle J(t) \rangle_T|$ is the complete relaxation (or decay) of $\operatorname{Re}\{C(t)\}$ before a typical correlation time, and the second condition is the faster decay of $\operatorname{Re}\{C(t)\}$ than $|\langle J(t) \rangle_T|$.

We plot the $\operatorname{Re}\{C(t)\}$ along with the $|J(t)|$ in Figure 2.8 in the low temperature limit, it is clear that the decay of $\operatorname{Re}\{C(t)\}$ is actually slower than that of $|J(t)|$ until around 4.8 fs. (In addition, of course $\operatorname{Re}\{C(t)\}$ never decays completely due to the finite number of normal modes.) Hence, over the short time that most of the decay occurs, one does not reach the exponential limit. The slower decay of $\operatorname{Re}\{C(t)\}$ in Figure 2.8 also explains the dominance of the initial Gaussian decay. When $\operatorname{Re}\{C(t)\}$ decays slowly, we can use $\operatorname{Re}\{C(t)\} \approx \operatorname{Re}\{C(0)\}$, and then $|\langle J(t) \rangle_T|$ can well be approximated as

$$|\langle J(t) \rangle_T| \approx \exp \left[- \frac{\langle (\delta \hat{U})^2 \rangle_T}{2\hbar^2} \operatorname{Re}\{C(0)\} t^2 \right]. \quad (2.39)$$

We also see from Figure 2.8 that the small time interval for the exponential decay accords with the time interval where $\operatorname{Re}\{C(t)\}$ has small values; because these conditions for the exponential decay are approximately satisfied in such time regions.

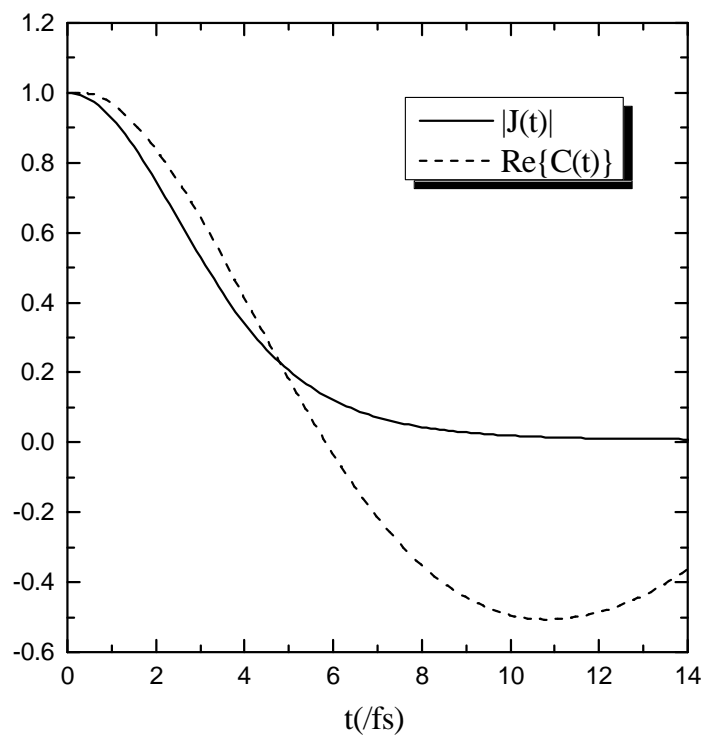


Figure 2.8: Decays of $|J(t)|$ and $\text{Re}\{C(t)\}$. Frequency shifts and Duschinsky rotation are included.

Electronic decoherence times can be defined perhaps most conventionally by

$$\tau_d = \int_0^\infty dt |J(t)|. \quad (2.40)$$

Using $|J^{ga}(t)|$ as the integrated function in Eq. (2.40), we define the resulting short-time approximate decoherence time as τ_d^{STA} . We present various decoherence times in Table 2.2. Table 2.2 shows that as the effects of frequency shifts and Duschinsky rotation are included (from model III to model I), the decoherence times become shorter. This is a reasonable result because non-totally symmetric modes can now participate in the decay of the canonical NOPF through frequency shifts and Duschinsky rotation. However, note an exception in τ_d^{exp} , which is only a local decay rate.

We next consider solvent effects. Prezhdo and Rossky [3] proposed a relationship between the electronic decoherence time scale and the energy gap fluctuation time scale in the high temperature limit, and estimated electronic decoherence times τ_D induced by only solvent molecules in several systems. In their study, decoherence times have been estimated as 4.5 fs for the first excited state of the hydrated electron in water, and to be 49 fs for the betaine-30 molecule in acetonitrile. If we assume that the vibrational coupling between the nuclei of a solute molecule and those of solvent molecules is small enough to be neglected and that the short time approximation is valid, the total decoherence time τ_D^{tot} can be decomposed into

$$\left(\frac{1}{\tau_D^{tot}}\right)^2 \approx \left(\frac{1}{\tau_D^{solut}}\right)^2 + \left(\frac{1}{\tau_D^{solv}}\right)^2, \quad (2.41)$$

Table 2.2: Various electronic decoherence times^a

	τ_D^{ga}	τ_d^{STA}	τ_d^{TI}	τ_d^{exp}
model I ^b	2.64	3.31	3.67	1.91
model II	2.71	3.40	3.72	1.85
model III	2.78	3.48	4.10	2.03

^aTemperature is fixed at 8K for the calculations of all the τ_D 's. Below are the definitions of the τ_D 's.

$$\begin{aligned}
 \bullet \tau_D^{ga} &\equiv -\frac{d^2}{dt^2} |\langle J(t) \rangle_T|_{t=0} & \bullet \tau_d^{STA} &= \int dt \exp \left[-\frac{1}{2} \frac{t^2}{(\tau_D^a)^2} \right] = \sqrt{\frac{\pi}{2}} \tau_D^{ga} \\
 \bullet \tau_d^{TI} &\equiv \int dt |\langle J(t) \rangle_T| & \bullet {}^c \tau_d^{exp} &\equiv \left[-\left\{ \frac{d}{dt} \ln |\langle J(t) \rangle_T| \right\}_{t=t_0} \right]^{-1}
 \end{aligned}$$

^bDefinitions for models are the same as in Fig. 5. See text.

^cIn principle, τ_d^{exp} should be calculated at $t = \infty$, but due to the phase recurrence, τ_d^{exp} is calculated at $t=t_0$. Here t_0 is the time where the exponential decay is most prominent. See text.

where τ_D^{solut} stands for the decoherence time induced by the nuclei of the solute, and τ_D^{solv} the time induced by the solvent molecules.

Taking into account that a betaine-30 molecule has a larger number of normal modes than the simplest betaine, it is a reasonable speculation that the electronic decoherence time by intramolecular vibrational motions in a betaine-30 should be no longer than 2.64 fs, which is the decoherence time in the simplest betaine. If we use the time 2.64 fs for the τ_D^{solut} and 49 fs for the τ_D^{solv} in a betaine-30/acetonitriles system in Eq. (2.41), we obtain the expected 2.64 fs for the total electronic decoherence time in the betaine-30/acetonitrile system. The total decoherence, which is essentially the same as the decoherence time due to the intramolecular vibrational modes, implies that the nuclear motions of a charge transfer polyatomic solute molecule such as a betaine molecule have far more effect on the total decoherence time than the nuclear motions of solvent molecules even in condensed phases.

2.4 Concluding remarks

We have carried out geometry optimization and vibrational normal mode analysis for the ground and the first excited states in the simplest betaine molecule. In our study, the most prominent difference between geometries of the two electronic state was the torsional angle which is attributed to the π to π^* transition. We have also shown that the frequencies of the torsional mode in the ground and the first excited state lie in the low frequency region, and the torsional mode is a nontotally symmetric mode. The inter-ring stretching mode frequencies in each state is not high due to the large masses of both rings. The Duschinsky matrix obtained is nearly diagonal, which suggests that Duschinsky rotation effects on electronic decoherence in this betaine molecule should be large

By using the nuclear overlap/phase function, we investigated electronic decoherence caused by intramolecular vibrational motions in the molecule. In our study, contributions to the decay of the canonical NOPF come from the harmonic vibrational motions, and the torsional motion is too slow to make a significant contribution to the decay. Frequency shifts have more influence on the decay of that function than Duschinsky rotation did, but the deviation from the simple spin-boson model by frequency shifts is also relatively small.

At longer times, we observed an exponential decay followed by phase recurrence in the decay of the canonical NOPF. This phase recurrence occurred due to the limited number of normal modes. Compared with the initial Gaussian decay, the exponential decay was not dominant. This was explained by

demonstrating that the condition for the exponential decay, i.e. fast and complete decay of the normalized energy gap fluctuation autocorrelation function, did not occur.

Through a short time (or Gaussian) approximation, we obtained an electronic decoherence time of 2.64 fs by the intramolecular vibrational motions in the betaine molecule. Decoherence times obtained with different approximations did not deviate from that time. Based on those times, we find that electronic decoherence by intramolecular vibrational motions occurs on an ultrafast time scale. The ultrafast decoherence time of 2.64 fs by intramolecular vibrational motions suggests that the nuclear motions of polyatomic solute molecules such as a betaine dye can have more effect on the total electronic decoherence than solvent molecules do. This reaches a conclusion that when we implement decoherence effect into an MQC-MD simulation on a polyatomic solute molecule in condensed phases, the incorporation of solely the decoherence effect from the solute molecule is sufficient to obtain a total decoherence time and thereby a reasonable NA transition rate.

Chapter 3

Harmonic model description of the Franck-Condon density for a betaine dye molecule

3.1 Introduction

Electron transfer (ET) reactions play an important role in many chemical and biological systems, and there have been many theoretical and experimental studies on ET reaction rates. [30, 89] A traditional and conventional approach to ET reaction rate is to neglect the dependence of electronic coupling matrix element on nuclear displacements (Condon approximation). [90] In that case, the ET reaction rate is factored into the purely electronic part and a purely nuclear part, the so called Franck-Condon (FC) factors. Due to the importance of the FC factors to ET reaction rates, many theoretical studies have been conducted to calculate the FC factors. Among several methods to the computation of FC factors, one direct approach is a sum-over-states method, which is normally based on recursion relations. [91, 92] Alternative time-dependent method has been developed by Heller. [26, 27, 93] In this method, the FC factors are not calculated directly, the FC envelop is the Fourier transform of the time-dependent overlap of two nuclear wave functions which are evolving on two different electronic potential energy surfaces (PES).

Sum-over-states method must be used for the direct calculation of FC factors, but there are some difficulties using that method for large molecules, since the equilibrium geometries of two electronic PES are in general rather different. That is, one PES is displaced with respect to the other PES, and frequencies on one PES are shifted from those in the other. Displacements occurs from the difference between minima of two PES's, and frequency shifts occur because one PES is distorted from the other. In addition, vibrational normal modes can change so that those in one electronic state are rotated or mixed in the normal mode basis of the other electronic state. This phenomenon, called a Duschinsky rotation or the Duschinsky effect, [71] prevents FC overlap integrals from being reduced to simple products of one-dimensional FC overlap integrals, and, as a result, the calculation of FC factors becomes more complicated. Due to the significance of FC factors, many methods for computing the integrals along with the Duschinsky rotation have been devised. [61, 94–101]. Sharp and Rosenstock have derived expressions based on a generating function method for computing the FC overlap integrals. [61] Gruner and Brumer have used a binary tree algorithm to develop an efficient technique to calculate the vibrational overlap integrals. [94]

As mentioned above, the sum-over-states method is based on recursion relations. [91], and efficient execution of recursion relations requires saving previous overlap integrals in computer memory. However, those methods are challenging to apply directly to large molecules since too many of FC overlap integrals must be saved in memory. To address this overflow problem, Ruhoff and Ratner proposed a three level-fixed binary tree (TLFBT) algorithm. [100]

This algorithm, discussed below, is based on the Gruner and Brumer’s binary tree algorithm, [94] but instead of building one large binary tree, binary trees for each level are constructed to reduce memory usage.

Among studied ET reactions is intramolecular ET, where the ET occurs within a single molecule. A good example of intramolecular ET reactions is that reaction occurring in the excited S_1 state of betaine dye molecules. Betaine dye molecules have drawn much attention from both experimental [46–53, 102–105] and theoretical community [39, 54–57] due to their distinct charge transfer absorption band and S_1 relaxation via back ET reaction that depend strongly on solvent polarity. Using transient absorption spectroscopy, Barbara and co-workers studied back ET reaction occurring in the betaine-30 molecule. [47–50] McHale and coworkers have studied intramolecular vibrational and solvent motions associated with charge transfer excitation in the betaine-30 using resonance Raman spectroscopy. [51, 102, 103] Werncke *et al.* investigated vibrational relaxation in the electronic ground state after intramolecular back ET by picosecond time-resolved anti-Stokes Raman spectroscopy. [52, 104, 105] Among computational studies on that dye molecule, Mente and Maroncelli carried out Monte Carlo simulations of the betaine-30 in various solvents to study the solvation dynamics. [55] Lobaugh and Rossky have investigated the dynamics of the first excited state of betaine-30 [56, 57] using mixed quantum/classical dynamics. [7]

In the present study, the simplest betaine, pyridinium-N-phenoxide betaine [4-(1-pyridinio)phenolate] is studied. As is shown in Figure 3.1, the molecule consists of a linked pyridinium ring and a phenoxide ring. The goal

is to examine methods for evaluating FC factors for a large molecule with the sum-over-states method and to investigate the properties of FC density functions obtained with different models.

We will employ harmonic potential energy surfaces, as has been used extensively for vibrational or vibronic spectrum calculations and ET reaction rate calculations. [58–60] We include a detailed consideration of frequency shifts and Duschinsky rotation, which can play an role in vibrational motions. [61–65] This generality allows us to study the importance of frequency shifts and Duschinsky rotation on FC factors. In general, one expects that a torsional motion cannot be described by a harmonic PES due to the softness and periodicity of that coordinate. In most treatment of a torsional motion, a periodic potential energy function for the torsional PES is sought, and the torsional motion is considered as a wave packet evolving on the potential energy function.[66–68] We follow this methodology here, and by doing so, we also study the effect of the torsional motion on FC factors. By comparing FC density functions obtained from the sum-over-states method and the time-dependent method, we will examine the advantages of each method over the other. In particular, we will investigate the behavior of FC factors in the high frequency region, where the FC density function has contribution from a large number of FC factors. [106]

This work is organized as follows. In the next section, we discuss theoretical methods for computing FC factors and FC density functions for the harmonic and torsional motions. In section III, the calculation results are shown and discussed. Concluding remarks appear in the final section IV.

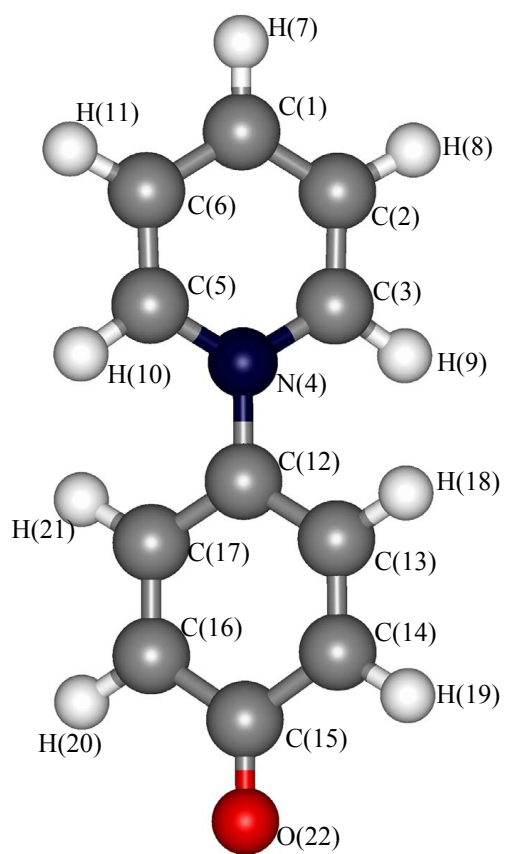


Figure 3.1: Molecular geometry and atom labelings of pyridinium-N-phenoxide betaine [4-(1-pyridinio)phenolate].

3.2 Theoretical methods

We begin by considering the ground and the first excited state of the simplest betaine molecule, in the gas phase. Considering ultrafast time scales of intramolecular vibrational motions, we make the reasonable and conventional assumption that the relaxation into the equilibrium geometry in the first excited state occurs rapidly after the electronic excitation. [49] We will primarily use a low temperature limit for calculations, corresponding to an initial state with the excited state vibrations all in their ground state. [64, 107] The model Hamiltonian of the system composed of these two electronic states can be expressed in terms of mass-weighted normal coordinates $\mathbf{Q} = \{Q_1, Q_2, \dots, Q_{3N-6}\}$ where N is the number of atoms in the molecule

$$\hat{H} = |g\rangle\hat{H}_g\langle g| + |e\rangle\hat{H}_e\langle e| + \gamma^\dagger|e\rangle\langle g| + \gamma|g\rangle\langle e|, \quad (3.1)$$

where $|g\rangle$ denotes the electronic ground state and $|e\rangle$ the first excited state. γ is an electronic coupling matrix element (assumed constant), while \hat{H}_g and \hat{H}_e are the nuclear Hamiltonians on electronic surfaces $|g\rangle$ and $|e\rangle$, respectively

$$\hat{H}_g = \hat{T}(\dot{\mathbf{Q}}_g) + \hat{V}_g(\mathbf{Q}_g), \quad (3.2a)$$

$$\hat{H}_e = \hat{T}(\dot{\mathbf{Q}}_e) + \hat{V}_e(\mathbf{Q}_e), \quad (3.2b)$$

Here \hat{T} and \hat{V} are the kinetic and the potential energy operators, respectively.

The Golden Rule transition rate from the first excited state to the ground state is expressed with FC factors as [106] :

$$k_{ET} = \frac{2\pi\gamma^2}{\hbar} \sum_g FC(e; g)\delta(E_e - E_g). \quad (3.3)$$

Here $E_{e(g)}$ is the total energy in the first excited (ground) state. $FC(e; g)$ is the FC weight or the squared FC overlap integral for each final state g and is defined as

$$FC(e; g) = I(e; g)^2 = |\langle \chi_e(\mathbf{Q}_e) | \chi_g(\mathbf{Q}_g) \rangle|^2, \quad (3.4)$$

where $I(e; g)$ is the FC overlap integral and $\chi_{e(g)}(\mathbf{Q}_{e(g)})$ are nuclear vibrational eigenfunctions in the first excited (ground) state. From the practical point of view, FC density functions are more useful than individual FC factors due to the resolution limit. Assuming the lowest vibrational level initially in the first excited state, the FC density functions $\Sigma(\omega)$ can be expressed as [106]

$$\Sigma(\omega) = \frac{1}{\delta\omega} \sum_g I(0; g)^2, \quad (3.5)$$

where the sum is taken over the vibrational states in the electronic ground state within some energy range $\delta\omega$, namely, $|\omega - \omega^g| \leq \delta\omega/2$. Here $\hbar\omega^g$ represents the vibrational energy difference of the ground and the first excited vibronic states. For instance, $\omega^g = \sum_j n_j^g \omega_j^g + \Delta G$ for the spin-boson model (no frequency shifts or mode mixing), where n_j^g and ω_j^g are a j th vibrational quantum number and a j th frequency in the ground state, respectively, and ΔG is the potential energy minimum difference between two electronic states.

Up to this point, a general description for the FC density function has been provided. We now invoke some reasonable approximations for the calculation of that function. First, a harmonic PES is utilized for the vibrational motions other than the torsional motion. In many cases, spin-boson model [12] which only considers displacements in harmonic potentials is sufficient to describe a system. [69] In general, however, frequency shifts and mixing of modes

(Duschinsky rotation) must be taken into account to precisely explain the change of the vibrational normal modes accompanied by an electronic transition. [64, 65] The detailed procedure used to obtain frequency shifts and the Duschinsky rotation matrix is described in detail elsewhere. [69, 72] For the highly anharmonic torsional motion, we use a method that has been proposed by Seidner *et al* [66] and used popularly by others. [67, 68] This method will be described in detail in the second subsection.

We decompose the nuclear Hamiltonian in Eq. (3.1) as [70]

$$\hat{H} = \hat{H}^{har} + \hat{H}^{tor} \quad (3.6)$$

where \hat{H}^{har} means the Hamiltonian which describes all the vibrational motions subject to the harmonic potential approximation and \hat{H}^{tor} represents the Hamiltonian for the torsional motion. Assuming that the torsional motion decouples from the other modes, based on the time scale difference between slow torsional motions and other motions, the FC density function can be written as [27]

$$\Sigma^{tot}(\omega) = \int_{-\infty}^{\infty} d\omega' \Sigma^{har}(\omega - \omega') \Sigma^{tor}(\omega'). \quad (3.7)$$

where $\Sigma^{har}(\omega)$ is the FC density function for \hat{H}^{har} and $\Sigma^{tor}(\omega)$ that for \hat{H}^{tor} . Detailed expressions for $\Sigma^{har}(\omega)$ and $\Sigma^{tor}(\omega)$ as well as \hat{H}^{har} and \hat{H}^{tor} are provided next.

3.2.1 Franck-Condon density function for harmonic motions with frequency shifts and Duschinsky rotation matrix

We consider $3N - 7$, harmonic vibrational degrees of freedom, with the seventh degree of freedom excluded being the torsional degree of freedom. We

use mass-weighted normal coordinates denoted as $\mathbf{Q} = \{Q_1, Q_2, \dots, Q_{3N-7}\}$. The harmonic nuclear Hamiltonians in the two states differ by frequency shifts and Duschinsky rotation as well as the displacement of the equilibrium nuclear positions. The Hamiltonian is then given by

$$\hat{H}^{har} = |g\rangle \hat{H}_g^{har}(\mathbf{Q}_g) \langle g| + |e\rangle \hat{H}_e^{har}(\mathbf{Q}_e) \langle e| + \gamma^{har}(|g\rangle \langle e| + |e\rangle \langle g|), \quad (3.8)$$

where γ^{har} is assumed to be real and static and

$$\hat{H}_g^{har}(\mathbf{Q}_g) = \frac{1}{2} \dot{\mathbf{Q}}_g^T \dot{\mathbf{Q}}_g + \frac{1}{2} \mathbf{Q}_g^T \boldsymbol{\Omega}_g \mathbf{Q}_g. \quad (3.9a)$$

$$\hat{H}_e^{har}(\mathbf{Q}_e) = \frac{1}{2} \dot{\mathbf{Q}}_e^T \dot{\mathbf{Q}}_e + \frac{1}{2} \mathbf{Q}_e^T \boldsymbol{\Omega}_e \mathbf{Q}_e + \Delta G, \quad (3.9b)$$

Here $\boldsymbol{\Omega}_e$ and $\boldsymbol{\Omega}_g$ are diagonalized frequency matrices in each state and ΔG is the potential energy minimum difference between the two electronic states. \mathbf{Q}^T is the transpose of \mathbf{Q} .

To evaluate a FC overlap integral of $I^{har}(e, g) = \langle \chi_e^{har}(\mathbf{Q}_e) | \chi_g^{har}(\mathbf{Q}_g) \rangle$, we should express the coordinates of the ground state as the function of the coordinates of the first excited state. This can be accomplished by a linear combination [61, 69, 71]

$$\mathbf{Q}_g = \mathbf{D} \mathbf{Q}_e + \Delta \mathbf{Q}, \quad (3.10)$$

where \mathbf{D} is Duschinsky rotation matrix and $\Delta \mathbf{Q}$ means a mass-weighted displacement vector.

As discussed elsewhere, alternative methods to obtain \mathbf{D} and $\Delta \mathbf{Q}$ are available. [69, 72] We find that a method due to Lee *et al*, [69] in which the geometry optimization is only carried out for the initial electronic state and

the geometry of the final electronic state is estimated by projecting the force constant matrix (Hessian matrix) at the initial state optimized geometry. Reorganization energies obtained in this way compare favorably to those reorganization energies inferred from experimental and computational data as show in Table 3.1. In Table 3.1, the values in the present work are obtained from the simplest betaine and all the others come from the betaine-30. Among the experimental [49, 53, 103] and computational [55–57] results, Maroncelli and coworker’s work and Rossky and coworker’s work consider only the torsional motion for the low frequency intramolecular reorganization energy. In the present study, the reorganization energy for the low frequency vibrational modes include the reorganization energy from the modes whose frequency is less than 200 cm^{-1} as well as from the torsional mode. Method A in the Table I corresponds to the straightforward method and method B does to Lee *et al*’s method. Both methods in this work use the spin-boson model for the calculation of the reorganization energy. Compared with experimental data, Lee *et al*’s method (method B) provides a closer value to the experimental results than method A.

The need for this less intuitive approach results from the relatively large displacements in the present case.

Following Ref. [69], we first optimize the excited state and perform frequency analysis of that electronic state to obtain the $\mathbf{\Omega}_e$ and $3N \times (3N - 7)$ transformation matrix \mathbf{L}_e^{mx} , which transforms mass-weighted Cartesian coordinates into normal coordinates. Next we calculate the Hessian matrix and the mass-weighted force vector (gradient) of the ground state at the equilibrium

Table 3.1: Comparison between the computational experimental data for low frequency, high frequency, and total intramolecular reorganization energies for simplest betaine and betaine-30^a

	$\lambda_{low}(/cm^{-1})$	$\lambda_{high}(/cm^{-1})$	$\lambda_{tot}(/cm^{-1})$
this work A ^{b,c}	3055	19013	22068
this work B ^{b,d}	2130	3100	5230
Barbara ^e	1233	1276	3509
Maroncelli ^f	1100		
Rosky ^g	760		
McHale ^h	33	87	120
Ernsting ⁱ	1940	1430	3370

^a Only this work is on the simplest betaine. All the other studies are carried out on betaine-30.

^b Both methods are using the spin-boson model.

^c The reorganization energy calculation in this work A is based on the method mentioned as the straightforward method in text.

^d This calculation is based on the Lee and *et al*'s method.

^e Ref 49.

^f Ref 55.

^g Refs 56,57.

^h Ref 103.

ⁱ Ref 53.

position of the first excited state. The Duschinsky matrix D can then be evaluated from the Hessian matrix of the ground state in Cartesian coordinates. [39] The mass-weighted displacement vector $\Delta\mathbf{Q}$ can then be calculated.

Sharp and Rosenstock have derived a generating-function-based expression for FC factors. [61] Following their method, we reach the equation

$$\sum_{\mathbf{m}=\mathbf{0}}^{\infty} \sum_{\mathbf{n}=\mathbf{0}}^{\infty} \mathbf{T}^{\mathbf{m}} \mathbf{U}^{\mathbf{n}} \left(\frac{2^{\mathbf{m}} 2^{\mathbf{n}}}{\mathbf{m}! \mathbf{n}!} \right) I^{har}(\mathbf{m}, \mathbf{n}) =$$

$$I^{har}(\mathbf{0}, \mathbf{0}) \exp \left[-(\mathbf{T}^T \mathbf{A} \mathbf{T} + 2\mathbf{T}^T \mathbf{B}) - (\mathbf{U}^T \mathbf{C} \mathbf{U} + 2\mathbf{U}^T \mathbf{G}) + 2\mathbf{T}^T \mathbf{E} \mathbf{U} \right],$$
(3.11)

where \mathbf{T} and \mathbf{U} are dummy variable vectors.[61].

The matrices in Eq. (3.11) are given as

$$\mathbf{A} = \mathbf{I} - 2\mathbf{J}(\mathbf{J}^T \mathbf{J} + \mathbf{I})^{-1} \mathbf{J}^T, \quad (3.12a)$$

$$\mathbf{C} = \mathbf{I} - 2(\mathbf{J}^T \mathbf{J} + \mathbf{I})^{-1}, \quad (3.12b)$$

$$\mathbf{E} = 2(\mathbf{J}^T \mathbf{J} + \mathbf{I})^{-1} \mathbf{J}^T, \quad (3.12c)$$

and vectors as

$$\mathbf{B} = \left[\mathbf{J}(\mathbf{J}^T \mathbf{J} + \mathbf{I})^{-1} \mathbf{J}^T - \mathbf{I} \right] \Delta, \quad (3.13a)$$

$$\mathbf{G} = (\mathbf{J}^T \mathbf{J} + \mathbf{I})^{-1} \mathbf{J}^T \Delta. \quad (3.13b)$$

Here \mathbf{I} is the identity matrix and \mathbf{J} and a dimensionless vector Δ are defined

respectively as

$$\mathbf{J} = \mathbf{\Gamma}_g \mathbf{D} \mathbf{\Gamma}_e^{-1}, \quad (3.14a)$$

$$\mathbf{\Delta} = \mathbf{\Gamma}_g \mathbf{\Delta} \mathbf{Q}, \quad (3.14b)$$

where an element of the diagonal matrix $\mathbf{\Gamma}_g$ is given as

$$(\mathbf{\Gamma}_g)_{jj} = \sqrt{\frac{\omega_j^g}{\hbar}}. \quad (3.15)$$

In addition, $I^{har}(\mathbf{0}, \mathbf{0})$ in Eq. (3.11) is given as

$$\begin{aligned} I^{har}(\mathbf{0}, \mathbf{0}) &= 2^{(3N-7)/2} \left[\det(\mathbf{J}^T \mathbf{J} + \mathbf{I}) \right]^{-\frac{1}{2}} \\ &\times \exp \left[-\frac{1}{2} \mathbf{\Delta}^T \mathbf{\Delta} + \frac{1}{2} \mathbf{\Delta}^T \mathbf{J} (\mathbf{J}^T \mathbf{J} + \mathbf{I})^{-1} \mathbf{J}^T \mathbf{\Delta} \right], \quad (3.16) \end{aligned}$$

where $\mathbf{0} = (0_1, 0_2, \dots, 0_k, \dots, 0_{3N-7})$.

Many conventional methods use the general recursion relation to calculate multidimensional FC overlap integrals. [61, 94–98] In our case, we derive a recursion relations from Eq. (3.11), which leads to

$$\begin{aligned} I^{har}(\mathbf{m}, \mathbf{n} + \mathbf{1}_k) &= - \sum_{j=1}^{3N-7} c_{kj} \left(\frac{n_j}{n_k + 1} \right)^{\frac{1}{2}} I^{har}(\mathbf{m}, \mathbf{n} - \mathbf{1}_j) \\ &\quad - d_k \left(\frac{2}{n_k + 1} \right)^{\frac{1}{2}} I^{har}(\mathbf{m}, \mathbf{n}) \\ &\quad + \sum_{j=1}^{3N-7} e_{kj} \left(\frac{m_j}{n_k + 1} \right)^{\frac{1}{2}} I^{har}(\mathbf{m} - \mathbf{1}_j, \mathbf{n}), \quad (3.17) \end{aligned}$$

where $\mathbf{n} = (n_1, n_2, n_3, \dots, n_{3N-7})$ and $\mathbf{1}_k = (0_1, 0_2, \dots, 1_k, \dots, 0_{3N-7})$.

Since we have assumed that the excited state vibrations are in their ground state (namely $\mathbf{m} = \mathbf{0}$), Eq. (3.17) is simplified into

$$I^{har}(\mathbf{0}, \mathbf{n} + \mathbf{1}_k) = - \sum_{j=1}^{3N-7} c_{kj} \left(\frac{n_j}{n_k + 1} \right)^{\frac{1}{2}} I^{har}(\mathbf{0}, \mathbf{n} - \mathbf{1}_j) - d_k \left(\frac{2}{n_k + 1} \right)^{\frac{1}{2}} I^{har}(\mathbf{0}, \mathbf{n}). \quad (3.18)$$

The straightforward recursion relation method requires large amounts of memory limiting their applications. [94, 100] In order to overcome this problem, Ruhoff and Ratner [100] proposed the three level-fixed binary tree algorithm (TLFBT), which is based on Gruner and Brumer's binary tree algorithm. [94] In Gruner and Brumer's binary tree algorithm, one large binary tree grows to save FC factors. However, TLFBT method divides the large binary tree into smaller binary trees. Each binary tree is labeled by the level and stores only FC factors belong to the same level. Here the level L is defined as

$$L = 1 + \sum_{j=1}^{3N-7} n_j, \quad (3.19)$$

where n_j is the quantum number of the j -th normal mode. The TLFBT method uses the fact that only the previous two levels $L - 1$ and $L - 2$ are required to calculate an FC factor in the level L . Therefore, the method stores FC factors pertaining to just the previous two levels, greatly reducing the memory usage. Although the TLFBT algorithm is used for our study, the number of FC integrals to be computed is still large for 59 normal modes. To reduce the number of FC integrals, we modify the TLFBT method and use symmetry groups for vibrational normal modes in next.

In general, totally symmetric low frequency modes have large displacements, and therefore high quantum numbers in the low frequency modes should be included in the calculation of the FC factors. For totally symmetric high frequency modes, however, displacements are small and only a few terms in a progression are sufficient to be considered. Suppose the level L binary tree. In this binary tree, FC factors are computed up to L quanta of each mode. When L is large, the computation of a FC factor for a high frequency normal mode whose displacement is small, wastes time and memory space. To address the problem, our modified method separates modes whose displacements are large from the other modes. First, FC factors for the large displacement modes are calculated, and then the binary trees grow up from each of the FC factors for the large displacement modes. For example, suppose that among totally symmetric modes we have 4 frequency modes which have large displacements and we should consider quantum numbers up to N_1 , N_2 , N_3 , and N_4 quanta for the 4 modes, respectively. Then, one first calculate FC factors the total number of which is $N_1 \times N_2 \times N_3 \times N_4$. Next levels is decided from the quantum numbers of only the other modes and binary trees grow up from each of the FC factors computed from the 4 modes. We can label each binary tree as $(0, 0, 0, 0, 0)$, $(0, 0, 0, 0, 1)$, \dots , $(0, 0, 0, 0, L)$, $(1, 0, 0, 0, 0)$, \dots , (N_1, N_2, N_3, N_4, L) , where the first four numbers in the parenthesis are quantum numbers for the four large displacements modes, and the last number is the level for the other modes. Since we consider the modes whose displacements are large separately, we can keep the level small in this way.

In addition, we use vibrational symmetry groups of the simplest betaine

molecule. Vibrational normal modes in the first excited state belong to A' and A'' symmetries since the symmetry of the optimized geometry in the first excited state is C_s . Due to the symmetry, the Duschinsky matrix is block-diagonalized into two sub-matrices. (See Figure 3.2.) Then, each sub-matrix can be treated separately, and FC overlap integrals are factored into a product, which is given as

$$I^{har}(\mathbf{0}, \mathbf{n}) = I^{har}(\mathbf{0}, \mathbf{n}^{A'}) \times I^{har}(\mathbf{0}, \mathbf{n}^{A''}) \quad (3.20)$$

Here $\mathbf{n}^{A'}$ is defined as $\mathbf{n}^{A'} = (n_1^{A'}, \dots, n_{N_{A'}}^{A'})$ and $\mathbf{n}^{A''} = (n_1^{A''}, \dots, n_{N_{A''}}^{A''})$; $N_{A'}$ and $N_{A''}$ are the total number of modes pertaining to symmetric groups A' and A'' , respectively.

Under the assumption that the excited state vibrations are all in their ground state, the FC density function is now given as [106]

$$\Sigma^{har}(\omega) = \frac{1}{\delta\omega} \sum_k I^{har}(\omega^g)^2, \quad (3.21)$$

where the sum is taken over the vibrational states in the electronic ground state within a resolution $\delta\omega$, i.e., $|\omega - \omega^g| \leq \delta\omega/2$ and ω^g is defined as

$$\omega^g = \sum_{j=1}^{3N-7} n_j^g \omega_j^g + \Delta w_{ge}^{zpe} + \Delta G. \quad (3.22)$$

Here Δw_{ge}^{zpe} is the zero point energy difference between the ground and the first excited state, that is, $\Delta w_{ge}^{zpe} = w_g^{zpe} - w_e^{zpe}$.

3.2.2 Franck-Condon density function induced by torsional motion

As mentioned above, the central inter-ring torsional motion is well beyond a harmonic potential description, and the method introduced in the

previous section cannot be applied to this torsional motion. The alternative time-dependent method due to Heller *et al.*, [26, 27] yield the FC density function via a Fourier transform of the time-dependent overlap between two nuclear wave functions evolving on two different electronic PES's.

Following Heller's method, [26, 27] first we explicitly calculate the periodic torsional potential energy function for the torsional motion of the electronic ground state. The torsional dynamics is then described as a wave packet evolving on the periodic PES. The dynamics of that mode is obtained by solving directly the time-dependent Schrödinger equation (TDSE), as discussed elsewhere. [39, 66–68]

The initial nuclear wave function is in the equilibrium position of the first excited state, so that the harmonic potential can be used for the first excited state PES $V_e^{tor}(\theta)$ given as

$$V_e^{tor}(\theta) = \frac{1}{2} I^{tor} (\omega_e^{tor})^2 (\theta - \theta_0^e)^2, \quad (3.23)$$

where θ_0^e is the torsional angle at the equilibrium configuration of the first excited state and V_0^{tor} is the energy at the configuration. The explicit torsional PES for the ground state is necessary. In general, the PES for the torsional motion is given as [77]

$$V_g^{tor}(\theta) = \frac{1}{2} \sum_n V_n (1 - \cos\{n(\theta - \theta_0^g)\}), \quad (3.24)$$

where θ_0^g is the torsional angle at the equilibrium configuration of the ground state and n is an integer. We obtain parameters for the ground state torsional PES by fitting computed potential energies as a function of θ .

The FC density can be expressed as the Fourier transform of the overlap between the two nuclear wave functions evolving on the first excited and ground state [26, 27];

$$\Sigma^{tor}(\omega) = 2\text{Re} \int_0^\tau dt \langle \Psi_e^{tor}(t) | \Psi_g^{tor}(t) \rangle \exp(i\omega t), \quad (3.25)$$

where $\Psi_e^{tor}(t)$ and $\Psi_g^{tor}(t)$ are nuclear wave functions on the first excited and ground state, respectively, where $\Psi_g^{tor}(t) = \Psi_g^{tor}(t)$. The relation between τ in Eq. (3.25) and $\delta\omega$ in Eq. (3.21) is

$$\delta\omega = \frac{2\pi}{\tau}. \quad (3.26)$$

3.3 Results and discussion

Geometry optimizations and frequency analysis are performed with the GAUSSIAN 98 program. [80] The geometry optimization in the ground state is carried out at the Hartree-Fock level at with 6-31G* basis set. Configuration interaction singles (CIS) with the same basis set is used to optimize the first excited state. Frequencies in this paper are scaled with the factor of 0.91. [81] The geometry optimizations of the ground and the first excited state are performed without applying any symmetry at first, and then by applying C_2 symmetry for the ground and C_s for the first excited state. The torsional angle between the pyridinium ring and the phenoxide ring in the first excited state is held fixed at 90° under C_s symmetry. We found that the electronic energies under the symmetry were not significantly different from those without symmetry, so we have applied the symmetries in all of our calculations, reported here.

Table 3.2: 60 normal mode frequencies (cm^{-1}) and displacements in the ground and the first excited state under the symmetries^{a,b}

mode	ω_g	ω_e	ΔQ	mode	ω_g	ω_e	ΔQ	mode	ω_g	ω_e	ΔQ
1	69.5	28.1	-5.69	21	1266.3	1252.0	-0.03	41	369.2	352.0	0.00
2	282.6	201.5	1.56	22	1172.1	1285.0	0.03	42	402.6	425.5	0.00
3	294.4	280.0	0.21	23	1327.2	1344.0	-0.59	43	410.0	434.9	0.00
4	512.1	387.5	-0.36	24	1452.5	1427.2	0.03	44	466.1	544.0	0.00
5	435.7	457.0	-0.75	25	1436.2	1447.7	-0.30	45	620.1	635.3	0.00
6	556.5	538.3	0.19	26	1477.6	1478.4	0.29	46	874.1	737.2	0.00
7	616.0	594.8	0.06	27	1528.0	1535.8	0.06	47	686.4	745.1	0.00
8	683.7	631.1	-0.39	28	1622.7	1620.2	0.02	48	768.4	810.9	0.00
9	804.7	658.3	0.08	29	1670.2	1666.6	-0.99	49	838.9	876.7	0.00
10	699.4	692.2	0.39	30	1748.3	1746.3	0.30	50	1025.9	969.0	0.00
11	1000.7	720.8	-0.05	31	3092.9	3087.0	0.05	51	966.6	1018.7	0.00
12	765.9	771.3	0.51	32	3076.7	3102.3	0.06	52	960.8	1020.8	0.00
13	936.3	953.1	0.28	33	3074.8	3102.8	0.00	53	1155.1	1031.4	0.00
14	949.4	969.2	-0.54	34	3104.3	3119.7	-0.04	54	1115.2	1081.7	0.00
15	1047.3	972.7	0.19	35	3107.0	3121.4	0.06	55	901.7	1261.8	0.00
16	1006.6	999.4	0.36	36	3145.5	3128.4	0.02	56	1480.6	1291.5	0.00
17	1018.6	1008.2	-1.01	37	3181.5	3158.7	0.06	57	1337.5	1370.0	0.00
18	1061.5	1097.1	0.00	38	27.1	62.4	0.00	58	1522.8	1522.7	0.00
19	1145.5	1163.1	-0.16	39	56.5	121.6	0.00	59	3094.6	3089.1	0.00
20	1201.2	1206.5	0.70	40	154.0	170.5	0.00	60	3179.7	3154.4	0.00

^a Configuration interaction singles (CIS) with 6-31G* is used to perform a geometry optimization for the first excited state. The frequencies of the ground state is obtained at the optimized geometry of the first excited state by diagonalizing force constant matrix (Hessian matrix) of the ground state. Calculation for the force constant matrix is performed at Hartree-Fock level with 6-31G*. Frequency scaling factor is 0.91, and displacements are unitless. See text.

^bThe first 37 normal modes belong to the totally symmetry group, A' and the other 23 to the nontotally symmetric group, A''. Note that only the normal modes belonging to A' have displacements.

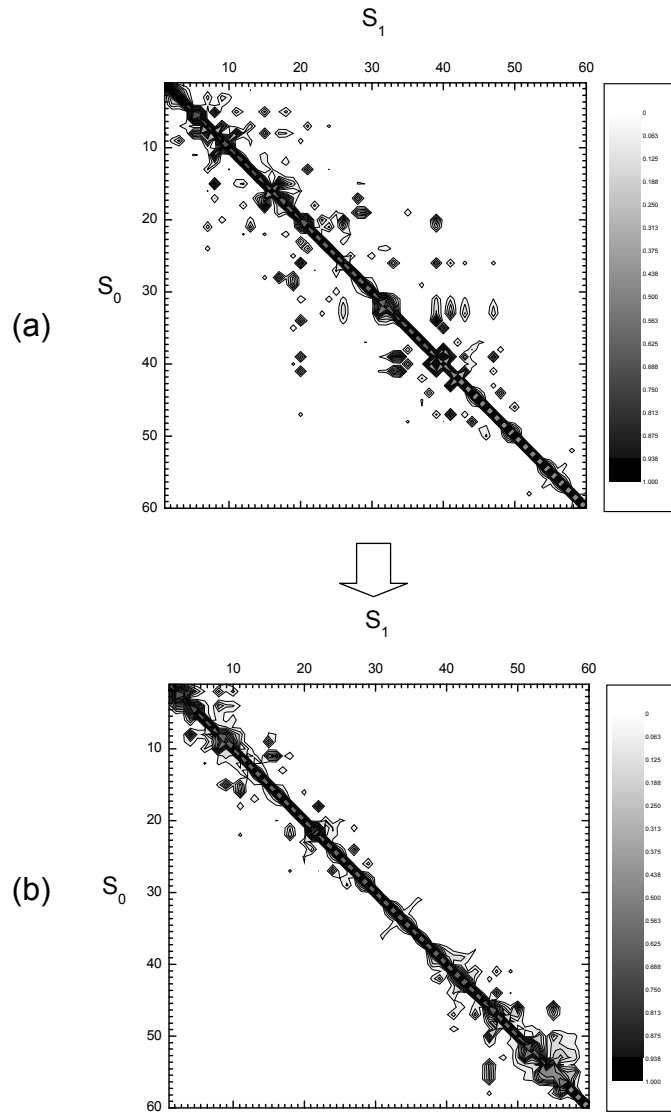


Figure 3.2: Absolute values of Duschinsky matrices' elements. (a) Normal modes in the ground (S_0) and the first excited state (S_1) are arranged in terms of the increasing order of frequencies. (b) Same as (a) except for being sorted by symmetry first, and then by frequency within the same symmetry. In (b), the modes 1 - 37 belong to symmetry A' and 38 - 60 to symmetry A'' .

Figure 3.2 shows Duschinsky rotation matrices ordered by frequency (Figure 3.2(a)) and after the blocking by vibrational symmetry groups, (Figure 3.2(b)). The first 37 normal modes belong to A' , and the other 23 to A'' , yielding the block-diagonalized Duschinsky matrix in Figure 3.2(b). Table 3.2 provides the frequencies and displacements which pertain to A' and A'' . Note that the normal modes pertaining to A'' symmetry group have zero displacements.

Before going further, it is worth commenting on the relation between these results and experimental resonance Raman observations. [51, 102, 103] Experiments (in solvent) showed that approximately 19 modes were resonance Raman active, among which 7 modes have prominent displacements (larger than 0.1). [103] Further, our study shows 18 normal modes whose displacements are relatively large (larger than 0.2). Among them, 9 modes have significant displacements larger than 0.5. Based on this observation, our study is in qualitative agreement with the resonance Raman study. Another agreement between our computational and the resonance Raman experimental study is about the relationship between frequencies and displacements. Both shows that displacements in the low frequency region are in general larger than in the high frequency region.

Figure 3.3 shows $\Sigma^{har}(\omega)$ for harmonic motions with varying $\delta\omega$ (see Eq. (3.5)). Frequency shifts and Duschinsky rotation are taken into account in the FC density spectra. Zero frequency in the graph corresponds to the minimum energy difference between the ground and first excited state PES's, i.e. zero corresponds to an energy difference of ΔG (see Eq. (3.9b)).

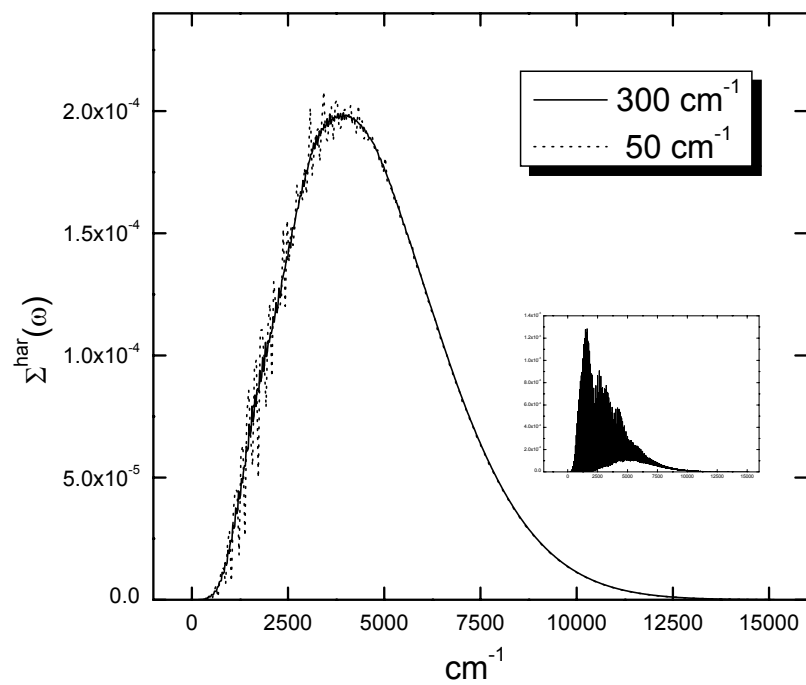


Figure 3.3: FC densities for the harmonic motions in the resolution of 300 cm^{-1} and 50 cm^{-1} . The inset shows the FC density in the resolution of 1 cm^{-1} . Both frequency shifts and Duschinsky rotation are included

The total number of FC factors computed is about 5.34×10^{14} , and the sum of FC factors is 0.9845. As quantum numbers increase or the level increases, the number of FC factors to be computed increases rapidly. The sharp increase makes it difficult to obtain FC factors in the high frequency region (or high quantum number), and, as a result, the total sum of FC factors is not exactly one. As $\delta\omega$ becomes small, more fine structure appears in the FC density function. It is interesting to note that at higher resolution, we can see irregular structure in the low frequency region, reflecting mode selectivity. [106] Mode selectivity occurs since only a few number of modes can contribute in the low frequency region. A distinct high frequency tail is also observed.

A FC density function for the harmonic motions can be also obtained from the Fourier transform of nuclear overlap/phase function (NOPF), i.e. with the time-dependent method outlined above. [26, 27, 93] The NOPF for the harmonic motion $J^{har}(t)$ is obtained analytically from the generating function method developed by Kubo-Toyozawa. [59] Then the FC density function can be directly calculated as:

$$\Sigma^{har}(\omega) = 2\text{Re} \int_0^\infty dt J^{har}(t) \exp(i\omega t), \quad (3.27)$$

where $J^{har}(t)$ is the NOPF for the harmonic motions.

In Figure 3.4, we show semilogarithmic plots of FC density function from the sum-over-states method and from the time-dependent method for the harmonic motions. Both frequency shifts and Duschinsky rotation are included in both cases, and $\delta\omega$ is 300 cm^{-1} corresponding to a τ (see Eq. (3.26)) of 111 fs. For this τ , $J^{har}(t) \sim 9.8 \times 10^{-7}$ In the low frequency region, the

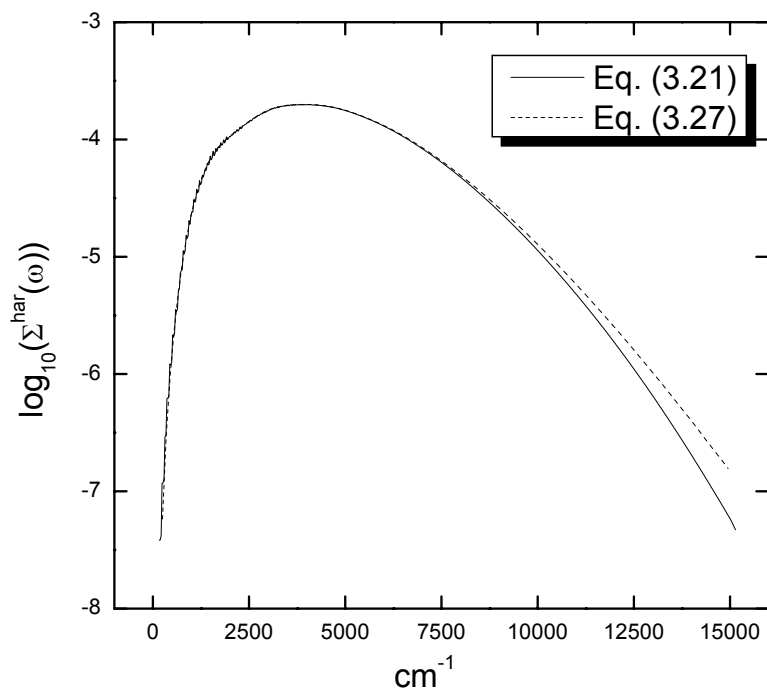


Figure 3.4: Semilogarithmic plot for the FC density functions comparing between the sum-over-states method and the time-dependent method for the harmonic motions. Both frequency shifts and Duschinsky rotation are included, and $\delta\omega = 300 \text{ cm}^{-1}$.

sum-over-states method shows a little mode selectivity, but the time-dependent method does not. In the high frequency region, however, due to the difficulty in the calculation of FC factors in the sum-over-states method, the result from the sum-over-states method becomes inaccurate and we can see the discrepancy between two methods. Thus the two approaches have complementary strengths.

In Figure 3.5, model I includes the effect of Duschinsky rotation as well as frequency shifts and displacements. While frequency shifts and displacements are considered in model II, model III accounts solely for the effect of displacements (spin-boson model). It is evident from Figure 3.5 that model II is somewhat different from model III, the differences originating from frequency shifts in the model II. A comparison between model I and model II shows that Duschinsky rotation has a relatively minor effect. Based on these observations, in our molecular system, frequency shifts introduce larger deviations from the spin-boson model than the Duschinsky rotation does.

It is evident that both frequency shifts and Duschinsky rotation increase values of the FC density function in the high frequency region. One reason of this is that nontotally symmetric modes which have no displacements can now affect the FC density function through frequency shifts and Duschinsky rotation. Sando *et al* studied the effects of Duschinsky rotation on an ET rate in a model system where two modes without displacements are mixed among eight modes. [64] They also observed the increased contribution to the ET rate from the high frequency region, and attributed the increase to the participation of the nontotally symmetric modes. We note that as frequency

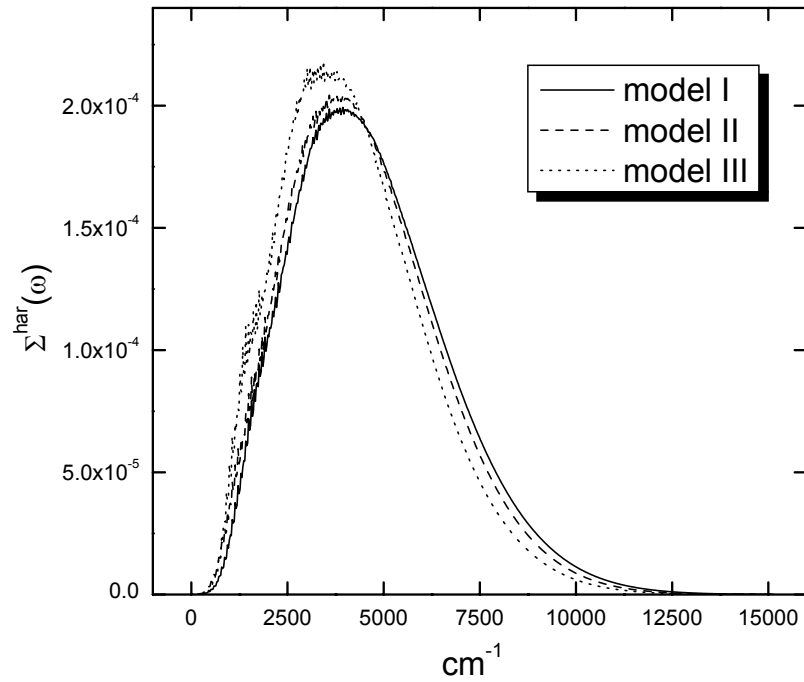


Figure 3.5: Comparison among several models for $\Sigma^{har}(\omega)$. Model I includes Duschinsky rotation and frequency shifts as well as displacements. In model II, Duschinsky rotation is not considered. Model III only has the effect of displacements. Both frequency shifts and Duschinsky rotation are included, and $\delta\omega = 300 \text{ cm}^{-1}$.

shifts and Duschinsky rotation are included, the number of FC factors to be computed are increased, i. e. the total number of FC factors goes from 8.86×10^{10} in model III, to 9.66×10^{12} in model II, to 5.34×10^{14} in model I. This increase also reflects the participation of nontotally symmetric modes.

As already mentioned previously, under the assumption of separable torsion from the other harmonic motions, the total FC density can be written as [27]

$$\Sigma^{tot}(\omega) = \int_{-\infty}^{\infty} d\omega' \Sigma^{har}(\omega - \omega') \Sigma^{tor}(\omega'), \quad (3.28a)$$

$$= \int_{-\infty}^{\infty} d\omega' \Sigma^{har}(\omega') \Sigma^{tor}(\omega - \omega'). \quad (3.28b)$$

Figure 3.6 shows the total FC density function as well as the FC density functions for the harmonic motions and for the torsional motion. The effects of frequency shifts and Duschinsky rotation are included. The calculation of the FC density function for the harmonic motions are performed using Eq. (3.5) and the FC density for the torsional motion is computed based on Eq. (3.25). The resolution is 300 cm^{-1} . It is clear that the role of the torsional motion is essentially to simply shift the peak of the spectra into a higher position.

One potentially interesting feature of the FC density function is the behavior of the function in the high frequency (or energy) region. [108, 109] Englman and Jortner showed that an exponential decay of the FC function can be expected from the spin-boson model in the weak coupling limit, defined as $\lambda_v \leq \hbar\langle\omega\rangle$. [109] Here the vibrational reorganization energy λ_v is given for

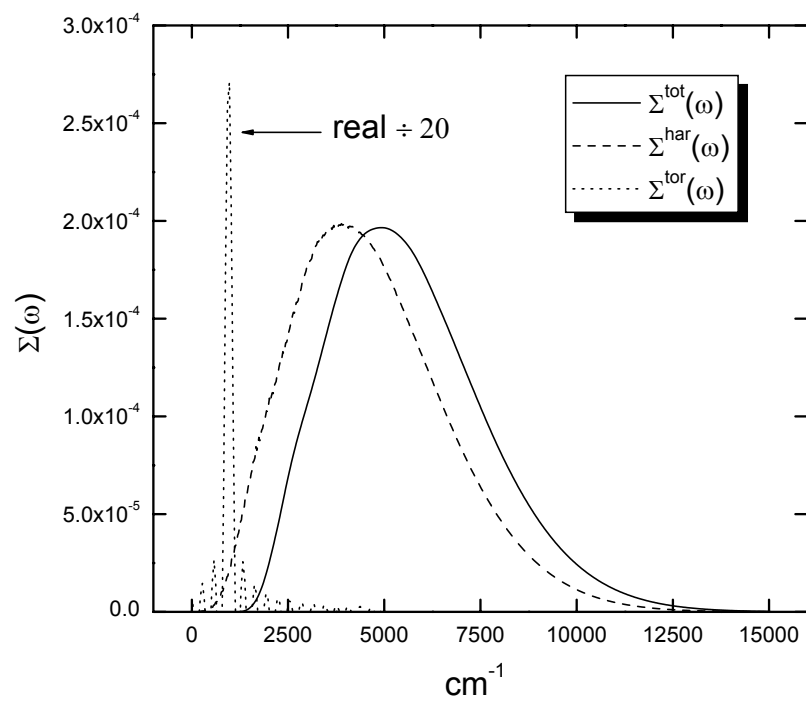


Figure 3.6: The total FC density, $\Sigma^{tot}(\omega)$ along with $\Sigma^{har}(\omega)$ and $\Sigma^{tor}(\omega)$. Both frequency shifts and Duschinsky rotation are included for $\Sigma^{har}(\omega)$, and $\delta\omega = 300 \text{ cm}^{-1}$.

harmonic model as

$$\lambda_v = \sum_j^{3N-7} \frac{1}{2} \Delta_j^2 \hbar \omega_j, \quad (3.29)$$

and the mean vibrational frequency is as

$$\langle \omega \rangle = \frac{\sum_j^{3N-7} \omega_j}{3N-6}, \quad (3.30)$$

In Figure 3.7, we present a semilogarithmic plot of the FC density function for the harmonic motions to examine the high frequency behavior in our system also for the spin-boson model (model III). For this purpose, we use the Fourier transform of the NOPF to obtain the FC density function at very high frequency. We use the spin-boson model to obtain the reorganization easily.

In Figure 3.7, we observe only a roughly exponential decay of very high energy. According to the Englman and Jortner's work, in order to observe a true exponential decay, the vibrational reorganization energy should be equal to or less than the mean vibration frequency. However, the vibrational reorganization energy of 4228 cm^{-1} in our system is much larger than the mean vibrational frequency of 1232 cm^{-1} . Due to the much larger reorganization energy than the mean vibrational frequency, our falls into the strong coupling limit, where the vibrational reorganization energy is larger than the mean vibrational frequency.

3.4 Concluding remarks

In this study, FC factors and FC density functions for the 60 vibrational modes of the simplest betaine molecule have been calculated by combination of the sum-over-states method and the time-dependent method. In

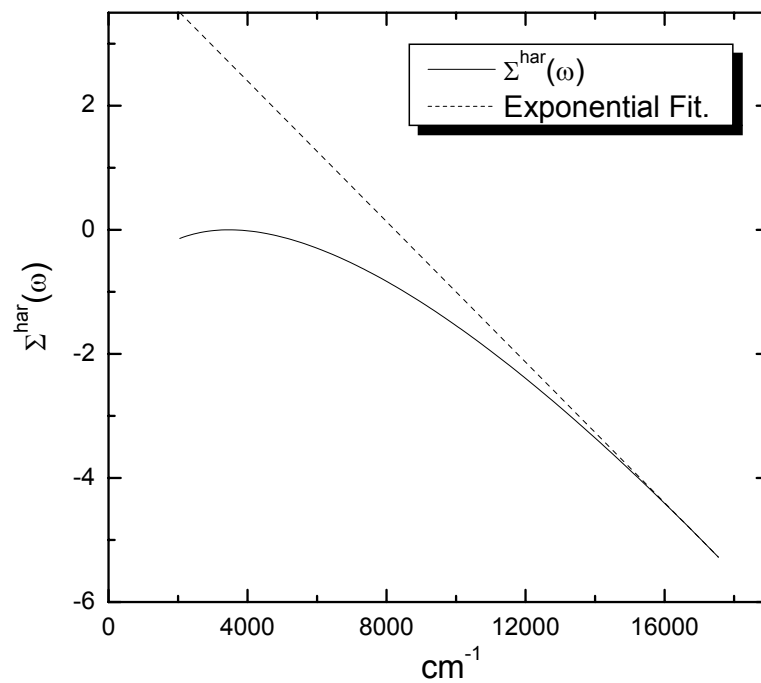


Figure 3.7: Semilogarithmic plot for the FC density function and exponential fit in the high frequency region to observe the exponential decay. For the easy calculation of vibrational reorganization energy, we use the spin-boson model for the FC density function. $\delta\omega = 300 \text{ cm}^{-1}$.

the sum-over-states method for the 59 harmonic motions, we were able to address the memory overflow problem by modifying the TLFBT algorithm and using the vibrational symmetry groups. The sum-over-states method agrees well with the time-dependent method except for the very high frequency region. Here, the rapid increase of the number of FC factors to be computed prevents a reasonable computation of all the FC factors required. In the low frequency region, the sum-over-states method reveals a fine structure reflecting some mode selectivity. Compared with experimental data from the resonance Raman experiments, displacement calculations in our study is in qualitative agreements with the experimental results. Both our study and the resonance Raman study also shows that low frequency modes have larger displacements than high frequency modes.

The inclusion of frequency shifts and Duschinsky rotation vastly increases the number of FC factors to be computed in the high frequency region. As a result, the FC density function becomes broader compared with the simple spin-boson model. We also observed that frequency shifts have more influence on the FC density function than Duschinsky rotation. The FC density function for the torsional motion has nearly a delta function-like shape, and so its role is solely to shift the position of the FC density function to a higher frequency. This is associated with the slow dynamics of torsion.

In the high frequency region, we did not observe strong exponential decay. For the simplest betaine molecule, the relatively large structural change between the ground and the first excited state leads to large displacements and the resulting large reorganization energy. As a result, the molecule falls into

the strong coupling limit, and an exponential decay energy gap law does not pertain.

When the low frequency region of FC density function for a large molecule is investigated, we find that the sum-over-states method readily provides fine structures. Due to the rapid increase in the number of contributing FC factors in the high frequency region and the resulting difficulty of computation, however, the sum-over-states method does not provide accurate values. In this case the time-dependent method is an excellent alternative.

Chapter 4

Derivation of quantum mechanical nuclear nonadiabatic coupling matrix elements using a spin-boson model

4.1 Introduction

Many chemical reactions occur through a transition between two different adiabatic potential energy surfaces, namely, a nonadiabatic (NA) transition and require a full quantum mechanical treatment to describe the transition. For chemical reactions occurring in the condensed phases, however, the full quantum mechanical treatment is intractable due to the tremendous computational effort. As an alternative, mixed quantum/classical molecular dynamics (MQC-MD) methods have been introduced. [7, 8, 33, 34, 110] In the MQC-MD methods, the dynamics of a small subsystem where a NA transition takes place is treated with a full quantum mechanical method, and the dynamics of a nuclear bath coupled to the subsystem is described with a classical method.

Among the MQC-MD methods is the Tully's surface hopping method, [7, 111] where the system evolves on one electronic surface at any time and hops stochastically between surfaces based on the state-to-state transition amplitudes. Due to the straightforwardness and advantages over the quantum mechanical methods, the MQC-MD methods have been extensively used to investigate many chemical reactions occurring in the condensed phase. [56, 57, 112–

MQC-MD methods deal with nuclear motions classically. In surface hopping methods, the classical treatment of nuclear dynamics leads to classical nuclear NA coupling matrix elements in NA coupling term, which is given as [7]

$$-i\hbar\langle\phi_k|\frac{\partial\phi}{\partial t}\rangle = \dot{\mathbf{R}} \cdot \mathbf{d}_{kj}(\mathbf{R}), \quad (4.1)$$

where ϕ_k and ϕ_j are the electronic wave functions for the k -th and j -th potential energy surfaces, $\dot{\mathbf{R}}$ is a nuclear velocity, and $\mathbf{d}_{kj}(\mathbf{R})$ is an electronic NA coupling vector (or matrix elements). Eq. (4.1) shows that the nuclear NA coupling matrix elements corresponds to the nuclear velocities in the classical treatment of the matrix elements. When a system involves large masses and large velocities, quantum effects such as tunneling or electronic decoherence are diminished due to the shorter de Broglie wavelengths. In that system, the classical treatment of nuclear motions and nuclear NA coupling matrix elements will reproduce the full quantum mechanical results well. However, there are many chemical systems where the quantum mechanical description of nuclear motions are important. For example, many experiments showed that high frequency intramolecular vibrational motions participate in an NA transition (back electron transfer reaction) in a betaine-30 in solutions. [47–53] Due to their high frequencies, the modes should be treated quantum mechanically. The surface hopping method along with Eq. (4.1), which use the classical description of nuclear NA coupling matrix elements, will not be able to yield a proper NA transition rate. To address this problem, Lobaugh and Rossky [56, 57] derived a quantum mechanical version of the nuclear NA cou-

pling matrix elements for intramolecular nuclear vibrational motions. They also incorporated that result into the surface hopping method to investigate the NA transition in a betaine-30/acetonitrile system. They assumed in their derivation that potential energy surfaces for the intramolecular vibrational motions are harmonic potential surfaces without displacements, and nuclear wave functions in each potential energy surface are time-independent.

In the present study, we provide another quantum mechanical nuclear NA coupling matrix elements for the intramolecular vibrational motions. For this purpose, we use displaced harmonic potential energy surfaces, so-called the spin-boson model. We will not take into account frequency shifts or Duschinsky rotation here because Lee *et al*'s study [69] and our previous studies [39, 84] showed that frequency shifts and Duschinsky rotation [71] do not make significant difference compared with the spin-boson model. We consider the time-dependence of nuclear wave functions. This time-dependence description is needed since nuclear configurations in a MQC-MD method changes in each time. In the next section, we provide a new derivation for a quantum mechanical nuclear NA coupling matrix elements and give a short summary.

4.2 Quantum mechanical derivation of nuclear nonadiabatic coupling matrix elements

We begin by considering two electronic surfaces which are harmonic in the nuclear coordinates and differ only by displacement of the equilibrium nuclear positions. Since of particular interest is the NA coupling term due to the intramolecular vibrational motions, those two electronic states are cou-

pled through intramolecular vibrational modes, which are expressed by mass-weighted normal coordinates $\mathbf{Q} = \{Q_1, Q_2, \dots, Q_{3N-6}\}$, where N is the total number of atoms in a solute molecule. Much literature on reactions has been devoted to consideration of this spin-boson model [12] or displaced harmonic oscillator model, [13] due to its analytical and compact expressions for various quantities. Suppose that the Hamiltonian of a system is

$$\hat{H} = |i\rangle\hat{H}_i\langle i| + |f\rangle\hat{H}_f\langle f| + \hat{\gamma}^\dagger|i\rangle\langle f| + \hat{\gamma}|f\rangle\langle i|, \quad (4.2)$$

where $|i\rangle$ denotes the initial electronic state and $|f\rangle$ the final electronic state. The electronic coupling matrix element is denoted by $\hat{\gamma}$, while \hat{H}_i and \hat{H}_f are the nuclear Hamiltonians on electronic surfaces $|i\rangle$ and $|f\rangle$, respectively

$$\hat{H}_i = \sum_j \frac{\hbar^2}{2} \hat{P}_j^2 + \sum_j \frac{1}{2} \omega_j^2 \hat{Q}_j^2, \quad (4.3a)$$

$$\hat{H}_f = \sum_j \frac{\hbar^2}{2} \hat{P}_j^2 + \sum_j \frac{1}{2} \omega_j^2 (\hat{Q}_j - D_j)^2 + E_0. \quad (4.3b)$$

Here, the index j denotes each nuclear coordinate, with frequency ω_j , coordinate displacement between two states specified by D_j , and a energy splitting specified by E_0 . Mass-weighted normal coordinate and conjugated momentum operators \hat{Q}_j and \hat{P}_j are used for convenience.

An NA coupling term due to the intramolecular degrees of freedom for

the electronic states can be expressed [56, 115]

$$\begin{aligned}
V_{if} &= \left\langle \Omega_i(\mathbf{Q}, t) \left\langle \Phi_i(\mathbf{Q}, \mathbf{r}) \left| \sum_j -\frac{\hbar^2}{2} \frac{\partial^2}{\partial Q_j^2} \right| \Phi_f(\mathbf{Q}, \mathbf{r}) \right\rangle_{\mathbf{r}} \right| \Omega_f(\mathbf{Q}, t) \right\rangle_{\mathbf{Q}} \quad (4.4a) \\
&= - \sum_j \hbar^2 \left\{ \left\langle \Omega_i(\mathbf{Q}, t) \left| \left\langle \Phi_i(\mathbf{Q}, \mathbf{r}) \left| \frac{\partial \Phi_f(\mathbf{Q}, \mathbf{r})}{\partial Q_j} \right\rangle_{\mathbf{r}} \right| \frac{\partial \Omega_f(\mathbf{Q}, t)}{\partial Q_j} \right\rangle_{\mathbf{Q}} \right. \right. \\
&\quad \left. \left. + \frac{1}{2} \left\langle \Omega_f(\mathbf{Q}, t) \left| \left\langle \Phi_i(\mathbf{Q}, \mathbf{r}) \left| \frac{\partial^2 \Phi_f(\mathbf{Q}, \mathbf{r})}{\partial Q_j^2} \right\rangle_{\mathbf{r}} \right| \Omega_f(\mathbf{Q}, t) \right\rangle_{\mathbf{Q}} \right\}. \quad (4.4b)
\end{aligned}$$

where \mathbf{Q} and \mathbf{r} represent a set of normal coordinates $\mathbf{Q} = \{Q_1, Q_2, \dots, Q_N\}$ and a set of electronic coordinates $\mathbf{r} = \{r_1, r_2, \dots\}$, respectively. $\langle \dots \rangle_{\mathbf{r}}$ and $\langle \dots \rangle_{\mathbf{Q}}$ mean the integrations with respect to the \mathbf{r} and \mathbf{Q} , respectively. We make an assumption that the first derivative of the initial electronic state varies slowly with \mathbf{Q} . We also invoke the Condon approximation, [90] which states that the electronic coupling matrix elements do not depend on nuclear coordinates. We can then ignore the second term of Eq. (4.4b), which, with the Condon approximation, yields

$$\begin{aligned}
V_{if} &\approx - \sum_j \hbar^2 \left\langle \Omega_i(\mathbf{Q}, t) \left| \left\langle \Phi_i(\mathbf{Q}, \mathbf{r}) \left| \frac{\partial \Phi_f(\mathbf{Q}, \mathbf{r})}{\partial Q_j} \right\rangle_{\mathbf{r}} \right| \frac{\partial \Omega_f(\mathbf{Q}, t)}{\partial Q_j} \right\rangle_{\mathbf{Q}}, \quad (4.5a) \\
&\approx - \sum_j^{3N-6} \hbar^2 \left\langle \Phi_i(\mathbf{Q}^0, \mathbf{r}) \left| \frac{\partial}{\partial Q_j} \right| \Phi_f(\mathbf{Q}^0, \mathbf{r}) \right\rangle \left\langle \Omega_i(\mathbf{Q}, t) \left| \frac{\partial}{\partial Q_j} \right| \Omega_f(\mathbf{Q}, t) \right\rangle, \quad (4.5b)
\end{aligned}$$

where \mathbf{Q}^0 means the nuclear configuration in a reference geometry. We drop the coordinate dependence of the integrations in Eq. (4.5b). Eq. (4.5b) shows that the NA coupling term can be expressed as the sum of the products

of electronic NA coupling matrix elements and nuclear NA coupling matrix elements. One issue associated with Eq. (4.5b) is that we should select a geometry as an reference. For example, suppose that we investigate an NA transition after an electronic excitation of the ground state. In case that the relaxation of nuclear motions after the excitation is very slow, we can consider that of the equilibrium ground state as a reference geometry. On the contrary, if the nuclear relaxation is fast enough to reach the equilibrium geometry of the excited state quickly, we can select the equilibrium excited state as a reference geometry.

First, we focus on the quantum mechanical expression for the nuclear NA coupling matrix element associated with the j -th normal mode. To do this, we introduce dimensionless quantities, \mathbf{q} and \mathbf{p} , which are defined as $q_j = \sqrt{\frac{\hbar}{\omega_j}} Q_j$ and $p_j = \sqrt{\frac{\hbar}{\omega_j}} P_j$ for convenience. The nuclear NA coupling matrix element with respect to the j -th dimensionless normal coordinate and the j -th momentum can be expressed as

$$\left\langle \Omega_i(\mathbf{Q}, t) \left| \frac{\partial}{\partial Q_j} \right| \Omega_f(\mathbf{Q}, t) \right\rangle = \sqrt{\frac{\omega_j}{\hbar}} \left\langle \Omega_i(\mathbf{q}, t) \left| \frac{\partial}{\partial q_j} \right| \Omega_f(\mathbf{q}, t) \right\rangle. \quad (4.6)$$

Due to the time-dependence of the nuclear wave functions in the Eq. (4.6), we should specify the initial condition for the nuclear wave functions. Here we use the thermally averaged nuclear configuration as an initial condition. Then, $\langle \Omega_i(\mathbf{q}, t) \left| \frac{\partial}{\partial q_j} \right| \Omega_f(\mathbf{q}, t) \rangle_T$ can be expressed by using the Feynman path integral formalism [116, 117] as

$$\langle \Omega_i(\mathbf{q}, t) \left| \frac{\partial}{\partial q_j} \right| \Omega_f(\mathbf{q}, t) \rangle_T = \frac{\int_{-\infty}^{\infty} d\mathbf{q} \int_{-\infty}^{\infty} d\mathbf{q}' \langle \mathbf{q}' | e^{-(\beta-\lambda)\hat{H}_i} | \mathbf{q} \rangle \frac{\partial}{\partial q_j} \langle \mathbf{q} | e^{-\lambda\hat{H}_f} | \mathbf{q}' \rangle}{\int_{-\infty}^{\infty} d\mathbf{q} \langle \mathbf{q} | e^{-\beta\hat{H}_i} | \mathbf{q} \rangle}, \quad (4.7)$$

where $\lambda = it/\hbar$. When Eq. (4.3) is used as the initial and final state Hamiltonians, the numerator in Eq. (4.7) can be given as

$$\begin{aligned}
& \int_{-\infty}^{\infty} d\mathbf{q} \int_{-\infty}^{\infty} d\mathbf{q}' \langle \mathbf{q}' | e^{-(\beta-\lambda)\hat{H}_i} | \mathbf{q} \rangle \frac{\partial}{\partial q_j} \langle \mathbf{q} | e^{-\lambda\hat{H}_f} | \mathbf{q}' \rangle \quad (4.8) \\
&= \frac{\Delta_j}{2i} \{ \cosh(\beta\hbar\omega_j/2)(1 - \cos(\omega_j t)) + i \sin(\omega_j t) \} \\
&\times \exp \left[- \sum_j \frac{\Delta_j^2}{2} \{ \cosh(\beta\hbar\omega_j/2)(1 - \cos(\omega_j t)) + i \sin(\omega_j t) \} - \frac{i}{\hbar} E_0 t \right] \\
&\times \prod_j \frac{1}{2|\sinh(\beta\hbar\omega_j/2)|}, \quad (4.9)
\end{aligned}$$

where $\Delta_j = \sqrt{\frac{\hbar}{\omega_j}} D_j$. Since the denominator in Eq. (4.7) is obtained easily as

$$\int_{-\infty}^{\infty} d\mathbf{q} \langle \mathbf{q} | e^{-\beta\hat{H}_i} | \mathbf{q} \rangle = \prod_j \frac{1}{2|\sinh(\beta\hbar\omega_j/2)|}, \quad (4.10)$$

Eq. (4.7) becomes

$$\begin{aligned}
& \langle \Omega_i(\mathbf{q}, t) | \frac{\partial}{\partial q_j} | \Omega_f(\mathbf{q}, t) \rangle_T \\
&= \frac{\Delta_j}{2i} \{ \cosh(\beta\hbar\omega_j/2)(1 - \cos(\omega_j t)) + i \sin(\omega_j t) \} \\
&\times \exp \left[- \sum_j \frac{\Delta_j^2}{2} \{ \cosh(\beta\hbar\omega_j/2)(1 - \cos(\omega_j t)) + i \sin(\omega_j t) \} \right] \\
&\times \exp \left[- \frac{i}{\hbar} E_0 t \right]. \quad (4.11)
\end{aligned}$$

Finally, inserting Eq. (4.8) into Eq. (4.6) leads to a quantum mechanical

expression for the nuclear NA coupling matrix as

$$\begin{aligned}
& \langle \Omega_i(\mathbf{Q}, t) | \frac{\partial}{\partial Q_j} | \Omega_f(\mathbf{Q}, t) \rangle_T \\
&= \frac{D_j}{2i} \{ \cosh(\beta \hbar \omega_j / 2) (1 - \cos(\omega_j t)) + i \sin(\omega_j t) \} \\
&\times \exp \left[- \sum_j \frac{\Delta_j^2}{2} \{ \cosh(\beta \hbar \omega_j / 2) (1 - \cos(\omega_j t)) + i \sin(\omega_j t) \} \right] \\
&\times \exp \left[- \frac{i}{\hbar} E_0 t \right]. \tag{4.12}
\end{aligned}$$

One concern about Eq. (4.12) is the initial condition for the nuclear configuration. We used the thermally averaged nuclear configuration as an initial condition. When we consider a photoinduced electron transfer reaction, however, the initial nuclear configuration is no longer the thermally equilibrated state. Instead, the initial nuclear configuration is more likely to be a nonequilibrium state or a microcanonical equilibrium depending on the initial laser pulse for the excitation and the rate of the intramolecular vibrational relaxation. [118–121] The nuclear NA coupling matrix elements for the nonequilibrium or the microcanonical nuclear configuration requires further study.

On the other hand, the calculation of the electronic NA coupling matrix element associated with the j -th normal mode is performed by transforming the normal coordinates into the Cartesian coordination. The reason why we use the Cartesian coordinates is that most calculations including the electronic NA coupling matrix elements in the MQC-MD methods are carried out in the Cartesian coordinates. To transform the Cartesian coordinates, we introduce

the linear transformation matrix \mathbf{L} between the Cartesian displacement Coordinates and the normal modes, which is given as

$$\mathbf{Q} = \mathbf{L}^T \sqrt{\mathbf{M}}(\mathbf{R} - \mathbf{R}^0). \quad (4.13)$$

The electronic NA coupling matrix element associated with the j -th normal mode is then written as [56]

$$\left\langle \Phi_i(\mathbf{Q}^0, \mathbf{r}) \left| \frac{\partial}{\partial Q_j} \right| \Phi_f(\mathbf{Q}^0, \mathbf{r}) \right\rangle = \sum_k^{3N} \frac{(\mathbf{L}^T)_{jk}^{-1}}{\sqrt{M_k}} \left\langle \Phi_i(\mathbf{R}^0, \mathbf{r}) \left| \frac{\partial}{\partial R_k} \right| \Phi_f(\mathbf{R}^0, \mathbf{r}) \right\rangle. \quad (4.14)$$

Here \mathbf{L}^T is $(3N-6) \times 3N$ transformation matrix and \mathbf{M} is a $3N \times 3N$ diagonal mass matrix.

Combining Eq. (4.12) and Eq. (4.14) to calculate the NA coupling term V_{if} , We finally obtain

$$\begin{aligned} V_{if} &= \sum_j^{3N-6} \sum_k^{3N} \frac{D_j}{2i} \{ \cosh(\beta\hbar\omega_j/2)(1 - \cos(\omega_j t)) + i \sin(\omega_j t) \} \\ &\times \exp \left[- \sum_j \frac{\Delta_j^2}{2} \{ \cosh(\beta\hbar\omega_j/2)(1 - \cos(\omega_j t)) + i \sin(\omega_j t) \} \right] \\ &\times \exp \left[- \frac{i}{\hbar} E_0 t \right] \frac{(\mathbf{L}^T)_{jk}^{-1}}{\sqrt{M_k}} \left\langle \Phi_i(\mathbf{R}^0, \mathbf{r}) \left| \frac{\partial}{\partial R_k} \right| \Phi_f(\mathbf{R}^0, \mathbf{r}) \right\rangle. \quad (4.15) \end{aligned}$$

Eq. (4.15) shows the final form for nuclear NA coupling matrix elements. When intramolecular vibrational motions play an important role in NA transitions in a molecular system, which is investigated with an MQC-MD simulation, Eq. (4.15) can be incorporated into the MQC-MD simulation. It should be noted that our derivation is based on the Condon approximation,

namely, neglecting any vibronic coupling. In case vibronic coupling becomes important, alternative methods should be devised. For low frequency intramolecular vibrational motions, vibronic coupling can be realized by including the vibrations into the simulation classically instead of using Eq. (4.15). Since the low frequency vibrational motions have little quantum effects, this classical and explicit implementation of the vibrational motions will be a good alternative. For example, vibronic couplings due to torsional motions between the pyridinium ring and the phenoxide ring in a betaine-30 was implemented into an MQC-MD simulation by treating them classically. [56] In this case, the frequencies and displacements corresponding to the torsional motions should be removed in Eq. (4.15). For high frequency intramolecular vibrational motions, however, quantum effects can be important and the classical treatment of those motions are irrelevant. To deal with vibronic coupling for the high frequency modes, further study is needed to obtain a new equation showing the non-Condon effect. Until then, Eq. (4.15) can be used since the equation is based on the quantum mechanics.

Bibliography

- [1] M. Simonius. *Phys. Rev. Lett.* **40**, 980, 1978.
- [2] W. H. Zurek. *Phys. Today* **44**, 36, 1991.
- [3] O. Prezhdo and P. J. Rossky. *Phys. Rev. Lett.* **81**, 5294, 1998.
- [4] P. J. Rossky. In B. J. Berne, G. Ciccotti, and D. Coker, editors, *Classical and Quantum Dynamics in Condensed Phase Simulations*. World Scientific, Singapore, 1997.
- [5] D. M. Lockwood, H. Hwang, and P. J. Rossky. *Chem. Phys.* **268**, 285, 2001.
- [6] J. Gong and P. Brumer. *Phys. Rev. Lett.* **90**, 050402, 2003.
- [7] J. C. Tully. *J. Chem. Phys.* **93**, 1061, 1990.
- [8] O. Prezhdo and P. J. Rossky. *J. Chem. Phys.* **107**, 5863, 1997.
- [9] K. F. Wong and P. J. Rossky. *J. Chem. Phys.* **116**, 8418, 2002.
- [10] K. F. Wong and P. J. Rossky. *J. Chem. Phys.* **116**, 8429, 2002.
- [11] E. Wigner. *Phys. Rev.* **161**, 367, 1932.
- [12] A. J. Leggett, S. Chakravarty, A. T. Dorsey, M. P. Fisher, A. Garg, and W. Zwerger. *Rev. Mod. Phys.* **59**, 1, 1987.

- [13] A. Warshel and J. K. Hwang. *J. Chem. Phys.* **84**, 4938, 1986.
- [14] S. Mukamel. *Principles of Nonlinear Optical Spectroscopy*. Oxford University Press, Oxford, 1995.
- [15] R. Kubo. *J. Phys. Soc. Jap.* **17**, 1100, 1962.
- [16] M. Maroncelli, J. MacInnis, and G. R. Fleming. *Science* **243**, 1674, 1989.
- [17] R. M. Stratt and M. Cho. *J. Chem Phys.* **100**, 6700, 1994.
- [18] D. Reichman and R. Silbey. *J. Chem. Phys.* **105**, 10500, 1996.
- [19] In M. Abramowitz and I. A. Stegun, editors, *Handbook of Mathematical Functions*. Dover Publications, Inc., New York, 1972.
- [20] J. Tang and S. H. Lin. *J. Chem .Phys.* **107**, 3485, 1997.
- [21] M. R. Spiegel and J. Liu. *Mathematical Handbook of Formulas and Tables, 2nd Ed.* McGraw-Hill, New York, 1999.
- [22] A. Staib and D. Borgis. *J. Chem Phys.* **103**, 2642, 1995.
- [23] O. Prezhdo and P. J. Rossky. *J. Chem. Phys.* **100**, 17094, 1996.
- [24] G. R. Fleming and M. Cho. *Annu. Rev. Phys. Chem.* **47**, 109, 1996.
- [25] H. Kawamoto. *Prog. Theor. Phys.* **82**, 1044, 1989.
- [26] E. J. Heller. *J. Chem. Phys.* **68**, 2066, 1978.

- [27] E. J. Heller. *J. Chem. Phys.* **68**, 3891, 1978.
- [28] E. Neria and A. Nitzan. *J. Chem. Phys.* **99**, 1109, 1993.
- [29] S. A. Egorov, E. Rabani, and B. J. Berne. *J. Chem. Phys.* **110**, 5238, 1999.
- [30] J. R. Bolton, N. Mataga, and G. McLendon. In J. R. Bolton, N. Mataga, and G. McLendon, editors, *Electron Transfer in Inorganic, Organic, and Biological Systems*. American Chemical Society, Washington DC, 1991.
- [31] T. A. Link. In A. Muller, H. Ratajczaks, W. Junge, and E. Diemann, editors, *Electron and Proton Transfer in Chemistry and Biology*. Elsevier, Amsterdam, 1992.
- [32] K. F. Wong and P. J. Rossky. *J. Phys. Chem. A* **105**, 2546, 2001.
- [33] P. Ehrenfest. *Z. Phys* **45**, 455, 1927.
- [34] F. A. Webster, P. J. Rossky, and R. A. Friesner. *Comp. Phys. Comm.* **63**, 494, 1991.
- [35] E. R. Bittner and P. J. Rossky. *J. Chem. Phys.* **103**, 8130, 1995.
- [36] K. Wynne and R. M. Hochstrasser. *Adv. Chem. Phys.* **107**, 263, 1997.
- [37] D. M. Lockwood, Y.-K. Cheng, and P. J. Rossky. *Chem. Phys. Lett.* **345**, 159, 2001.
- [38] B. J. Schwartz and P. J. Rossky. *J. Chem. Phys.* **105**, 6997, 1996.

- [39] H. Hwang and P. J. Rossky. *To be submitted*.
- [40] R. A. Maradudin. *Solid State Phys.* **18**, 273, 1966.
- [41] J. L. Skinner and D. Hsu. *Adv. Chem. Phys.* **65**, 1, 1986.
- [42] J. L. Skinner. *J. Chem. Phys.* **77**, 3398, 1982.
- [43] D. Hsu and J. L. skinner. *J. Chem. Phys.* **81**, 1604, 1984.
- [44] J. L. Skinner and D. Hsu. *J. Phys. Chem.* **90**, 4931, 1986.
- [45] E. Neria and A. Nitzan. *Phys. Rev. Lett.* **67**, 1011, 1993.
- [46] C. Reichardt. *Angew. Chem. Int. Ed. Engl.* **18**, 98, 1979.
- [47] Eva Åkesson, G. C. Walker, and P. F. Barbara. *J. Chem. Phys.* **95**, 4188, 1991.
- [48] P. F. Barbara, G. C. Walker, and T. P. Smith. *Science* **256**, 975, 1992.
- [49] G. C. Walker, E. Åkesson, A. E. Johnson, N. E. Levinger, and P. F. Barbara. *J. Phys. Chem.* **96**, 3728, 1992.
- [50] P. J. Reid and P. F. Barbara. *J. Phys. Chem.* **99**, 3554, 1995.
- [51] Y. Zong and J. L. McHale. *J. Chem. Phys.* **106**, 4963, 1997.
- [52] S. Hogiu, J. Dreyer, M. Pfeiffer, K.-W. Brzezinka, and W. Werncke. *J. Raman Spectrosc.* **31**, 797, 2000.

- [53] S. A. Kovalenko, N. Eilers-König, T. A. Senyushkina, and N. P. Ernsting. *J. Phys. Chem. A* **105**, 4834, 2001.
- [54] W. Bartkowiak and L. Lipiński. *J. Phys. Chem. A* **1998**, 5236, 1998.
- [55] S. R. Mente and M. Maroncelli. *J. Phys. Chem. B* **103**, 7704, 1999.
- [56] J. Lobaugh and P. J. Rossky. *J. Phys. Chem. A* **103**, 9432, 1999.
- [57] J. Lobaugh and P. J. Rossky. *J. Phys. Chem. A* **104**, 899, 2000.
- [58] Jr. E. B. Wilson, J. C. Decius, and P. C. Cross. *Molecular Vibrations*. McGraw-Hill, New York, 1955.
- [59] R. Kubo and Y. Toyozawa. *Prog. Theor. Phys.* **13**, 160, 1955.
- [60] I. N. Levine. *Molecular spectroscopy*. John Wiley & Sons, New York, 1975.
- [61] T. E. Sharp and H. M. Rosenstock. *J. Chem. Phys.* **41**, 3453, 1964.
- [62] G. J. Small. *J. Chem. Phys.* **54**, 3300, 1971.
- [63] A. M. Mebel, M. Hayashi, K. K. Liang, and S. H. Lin. *J. Phys. Chem. A* **103**, 10674, 1999.
- [64] G. M. Sando, K. G. Spears, J. T. Hupp, and P. T. Ruhoff. *J. Phys. Chem.* **105**, 5317, 2001.
- [65] G. M. Sando and K. G. Spears. *J. Phys. Chem.* **105**, 5326, 2001.

- [66] L. Seidner and W. Domcke. *Chem. Phys.* **186**, 27, 1994.
- [67] Y. Chuang and D. G. Truhlar. *J. Chem. Phys.* **112**, 1221, 2000.
- [68] D. C. Clary. *J. Chem. Phys.* **114**, 9725, 2001.
- [69] E. Lee, E. S. Medvedev, and A. A. Stuchebrukhov. *J. Chem. Phys.* **112**, 9015, 2000.
- [70] H. Köppel, W. Domcke, and L. S. Cederbaum. *Adv. Chem. Phys.* **57**, 59, 1984.
- [71] F. Duschinsky. *Acta Physicochim. (USSR)* **7**, 551, 1937.
- [72] A. M. Mebel, Y.-T. Chen, and S.-H. Lin. *Chem. Phys. Lett.* **258**, 53, 1996.
- [73] A. Warshel and M. Karplus. *Chem. Phys. Lett.* **17**, 7, 1972.
- [74] A. Warshel. *J. Chem. Phys.* **62**, 214, 1975.
- [75] W. H. Press, S. A. Teukolsky, W. T. Vetterling, and B. P. Flannery. *Numerical Recipes in C, 2nd Ed.* Cambridge University Press, Cambridge, 1992.
- [76] S. A. Egorov, E. Rabani, and B. J. Berne. *J. Chem. Phys.* **108**, 1407, 1997.
- [77] W. E. Sinclair, H. Yu, and D. Phillips. *J. Chem. Phys.* **106**, 5797, 1997.

- [78] D. Kosloff and R. Kosloff. *J. Comput. Phys.* **52**, 35, 1983.
- [79] R. Kosloff. *Annu. Rev. Phys. Chem.* **45**, 145, 1994.
- [80] M. J. Frisch, G. W. Trucks, H. B. Schlegel, G. E. Scuseria, M. A. Robb, J. R. Cheeseman, V. G. Zakrzewski, J. A. Montgomery, Jr., R. E. Stratmann, J. C. Burant, S. Dapprich, J. M. Millam, A. D. Daniels, K. N. Kudin, M. C. Strain, O. Farkas, J. Tomasi, V. Barone, M. Cossi, R. Cammi, B. Mennucci, C. Pomelli, C. Adamo, S. Clifford, J. Ochterski, G. A. Petersson, P. Y. Ayala, Q. Cui, K. Morokuma, D. K. Malick, A. D. Rabuck, K. Raghavachari, J. B. Foresman, J. Cioslowski, J. V. Ortiz, A. G. Baboul, B. B. Stefanov, G. Liu, A. Liashenko, P. Piskorz, I. Komaromi, R. Gomperts, R. L. Martin, D. J. Fox, T. Keith, M. A. Al-Laham, C. Y. Peng, A. Nanayakkara, C. Gonzalez, M. Challacombe, P. M. W. Gill, B. Johnson, W. Chen, M. W. Wong, J. L. Andres, C. Gonzalez, M. Head-Gordon, E. S. Replogle, , and J. A. Pople. *Gaussian 98, Revision A.7*. Gaussian, Inc., Pittsburgh PA, 1998.
- [81] A. Scott and L. Radom. *J. Phys. Chem.* **100**, 16502, 1996.
- [82] T. Ishida and P. J. Rossky. *J. Phys. Chem. A* **105**, 558, 2001.
- [83] T. Ishida and P. J. Rossky. *To be submitted*, 2003.
- [84] H. Hwang and P. J. Rossky. *To be submitted*.
- [85] D. G. Evans and R. Coalson. *J. Chem. Phys.* **97**, 5081, 1992.

- [86] J. Cao, L. W. Ungar, and G. A. Voth. *J. Chem. Phys.* **104**, 4189, 1996.
- [87] A. G. Redfield. *Adv. Magn. Reson.* **1**, 1, 1966.
- [88] G. C. Schatz and M. A. Ratner. *Quantum Mechanics in Chemistry*. Prentice-Hall, Englewood Cliffs, New Jersey, 1993.
- [89] M. Bixon and J. Jortner. Electron transfer-from isolated molecules to biomolecules. In J. Jortner and M. Bixon, editors, *Electron Transfer-From Isolated Molecules to Biomolecules*. John Wiley & Sons, New York, 1999.
- [90] E. U. Condon. *Phys. Rev.* **32**, 858, 1928.
- [91] C. Manneback. *Physica* **17**, 1001, 1951.
- [92] A. B. Myers. Resonance raman intensities: A probe of excited-state structure and dynamics. In T. G. Spiro, editor, *Biological Application of Raman Spectroscopy (Vol. 2)*. Wiley, New York, 1987.
- [93] S.-Y. Lee and E. J. Heller. *J. Chem. Phys.* **71**, 4777, 1979.
- [94] D. Gruner and P. Brumer. *Chem. Phys. Lett.* **138**, 310, 1987.
- [95] J. Lermé. *Chem. Phys.* **145**, 67, 1990.
- [96] P. T. Ruhoff. *Chem. Phys.* **186**, 355, 1994.
- [97] A. Peluso, F. Santoro, and G. Del Re. *Int. J. Quant. Chem* **63**, 233, 1997.

- [98] P. Malmqvist and N. Forsberg. *Chem. Phys.* **228**, 227, 1989.
- [99] F. Iachello and M. Ibrahim. *J. Phys. Chem. A* **102**, 9427, 1998.
- [100] P. T. Ruhoff and M. A. Ratner. *Int. J. Quant. Chem.* **77**, 383, 2000.
- [101] A. Toniolo and M. Persico. *J. Comput. Chem.* **22**, 968, 2001.
- [102] Y. Zong and J. L. McHale. *J. Chem. Phys.* **107**, 2920, 1997.
- [103] X. Zhao, J. A. Burt, F. J. Knorr, and J. L. McHale. *J. Phys. Chem. A* **105**, 11110, 2001.
- [104] S. Hogiu, W. Werncke, M. Pfeiffer, and T. Elsaesser. *Chem. Phys. Lett.* **312**, 407, 1999.
- [105] S. Hogiu, W. Werncke, M. Pfeiffer, and J. Dreyer and T. Elsaesser. *J. Chem. Phys.* **113**, 1587, 2000.
- [106] M. Bixon and J. Jortner. *Chem. Phys.* **176**, 467, 1993.
- [107] S. Karabunarilev, M. Baumgarten, E. R. Bittner, and K. Müllen. *J. Chem. Phys.* **113**, 11372, 2000.
- [108] W. Siebrand. *J. Chem. Phys.* **44**, 4055, 1966.
- [109] R. Englman and J. Jortner. *Mol. Phys.* **18**, 145, 1970.
- [110] P. Pechukas. *Phys. Rev.* **181**, 166, 1969.
- [111] J. C. Tully. *Int. J. Quant. Chem. Symp.* **93**, 299, 1991.

- [112] S. Hammes-schiffer and J. C. tully. *J. Chem. Phys.* **101**, 4657, 1994.
- [113] J. Morelli and Sharon Hammes-Schiffer. *Chem. Phys. Lett.* **269**, 161, 1997.
- [114] J.-Y. Fang and S. Hammes-Schiffer. *J. Chem. Phys.* **107**, 8933, 1997.
- [115] M. Hayashi, A. M. Mebel, K. K. Liang, and S. H. Lin. *J. Chem. Phys.* **108**, 2044, 1998.
- [116] R. P. Feynman and A. R. Hibbs. McGraw-Hill, New York, 1965.
- [117] J. Tang. *Chem. Phys. Lett***227**, 170, 1994.
- [118] Y. J. Yan and S. Mukamel. *J. Chem. Phys.* **85**, 5908, 1986.
- [119] H. Wadi and E. Pollak. *J. Chem. Phys.* **110**, 11890, 1999.
- [120] E. Pollak and Y. He. *J. Phys. Chem. B* **105**, 6500, 2001.
- [121] D. Schwarzer, C. Hanisch, P. Kutne, and J. Troe. *J. Phys. Chem. A* **106**, 8019, 2002.

Vita

Hyonseok Hwang was born in Kwan-In, Kyong-Ki Do, Republic of Korea on February 23, 1970, the son of Wonkon Hwang and Munja Lim. As soon as he received the Bachelor of Science degree in Chemistry at Seoul National University in 1995, he entered the same university for his Master of Science degree in Chemistry. After completing his Master degree program in 1997, he worked as a research assistant at the Research Institute of Basic Research for one year. He joined the graduate program in Chemistry at the University of Texas in September, 1998.

Permanent address: 670-1 Shin-Chul Won 2 Li Gal-Mal Yub,
Chul-Won Gun Kang-Won Do, 269-800,
Republic of Korea

This dissertation was typeset with \LaTeX^\dagger by the author.

[†] \LaTeX is a document preparation system developed by Leslie Lamport as a special version of Donald Knuth's \TeX Program.